

Journal Pre-proof

Shear-Driven Micro/Nano Flows Simulation using Fokker Planck Approach:
Investigating Accuracy and Efficiency

Vahid RezapourJaghargh, Amirmehran Mahdavi, Ehsan Roohi



PII: S0042-207X(19)32319-X

DOI: <https://doi.org/10.1016/j.vacuum.2019.109065>

Reference: VAC 109065

To appear in: *Vacuum*

Received Date: 12 September 2019

Revised Date: 6 November 2019

Accepted Date: 6 November 2019

Please cite this article as: RezapourJaghargh V, Mahdavi A, Roohi E, Shear-Driven Micro/Nano Flows Simulation using Fokker Planck Approach: Investigating Accuracy and Efficiency, *Vacuum*, <https://doi.org/10.1016/j.vacuum.2019.109065>.

This is a PDF file of an article that has undergone enhancements after acceptance, such as the addition of a cover page and metadata, and formatting for readability, but it is not yet the definitive version of record. This version will undergo additional copyediting, typesetting and review before it is published in its final form, but we are providing this version to give early visibility of the article. Please note that, during the production process, errors may be discovered which could affect the content, and all legal disclaimers that apply to the journal pertain.

© 2019 Elsevier Ltd. All rights reserved.

Shear-Driven Micro/Nano Flows Simulation using Fokker Planck

Approach: Investigating Accuracy and Efficiency

Vahid RezapourJaghargh¹, Amirmehran Mahdavi¹, Ehsan Roohi^{1,2,*}

¹Department of Mechanical Engineering, Faculty of Engineering, Ferdowsi University of Mashhad, P.O. Box 91775-1111, Mashhad, Iran

²International Center for Applied Mechanics (ICAM), School of Aerospace Engineering, Xi'an Jiaotong University (XJTU), Xi'an, China

Abstract

A detailed study on the performance and accuracy of the Fokker Planck (FP) approach in treating shear driven flows over a wide range of Knudsen numbers and Mach numbers at subsonic and supersonic regimes is considered. One-dimensional Couette flow and the two-dimensional cavity problem are considered. The FP method is evaluated in the Couette flow at a subsonic Mach number of 0.16 ($U_w=50$ m/s) and at the supersonic Mach number of 3.1 ($U_w=1000$ m/s), where Knudsen numbers range from 0.005 to 1. Correspondingly, the cavity flow is investigated at a wall Mach number of 0.31 ($U_w=100$ m/s) and wall Mach number of 0.93 ($U_w=300$ m/s) at Knudsen numbers ranging from 0.05 to 20. Interestingly, the results show that by increasing the wall velocity and Knudsen numbers, the accuracy of the FP approach increases in treating the cavity flow. In addition to the standard Knudsen number, we show that gradient length Knudsen number, Kn_{GL} , should be considered to determine the range of accuracy of the FP scheme. The latter depends on the strength of the center vortex of the cavity diminishing at higher rarefied conditions. The results demonstrate that the computational efficiency of the FP approach enhances at higher lid velocity.

Keywords: Fokker Planck approach, Rarefied flows, Knudsen number, Shear-driven flow, Micro/nanoflow.

* Email: Corresponding author, email: e.roohi@um.ac.ir

1. Introduction

Investigation of micro-nano flows attracted attention of researchers during the last three decades. Flows at small scale geometries usually experience rarefied conditions. Flow rarefaction is expressed in term of the Knudsen number (Kn), that is defined as:

$$Kn = \frac{\lambda}{L} \quad (1)$$

, where λ and L are the molecular mean free path and the characteristic length of the flow conduit, respectively. Depending on the degree of the rarefaction, different flow regimes were considered [1]–[3]. $Kn < 0.001$ is categorized as the continuum (non-slip) regime, $0.001 < Kn < 0.1$ is the slip regime, $0.1 < Kn < 10$ is transitional regime and $Kn > 10$ is considered as free molecular regime [4].

Direct simulation Monte Carlo method (DSMC) was introduced to simulate rarefied gas flow in the early 60's by Bird [5]. In this method, flow analysis is made possible by simulating the movement and collision of a series of representative gas particles. Although the method has a very suitable efficiency at higher Knudsen numbers, it is time-consuming at lower Knudsen numbers.

The Fokker Planck (FP) method was first examined by Kirkwood for liquids [6]. The application of this method is for high-density flows. This method was later developed by Cercignani for dense gases [7]. Jenny et al. [8] extended the method for rarefied gases and presented a statistical algorithm based on the FP approximation. Their results were very consistent with the DSMC, Boltzmann linearized equation, and experimental data. Nevertheless, the heat transfer and temperature were miscalculated, because of wrong Prandtl number. Gorji et al. developed an algorithm to solve the problem of wrong Prandtl number by introducing a cubic drift term [9]. Thus, their results led to correct Prandtl number and heat transfer. They showed the accuracy of this model for various test cases [10]. Singh proposed an FP equation to fix the Prandtl number problem [11]. Later, the FP model was extended for mixtures [12] and polyatomic gas [13]–[16].

FP models were suggested for studying rarefied gas flow simulations [17]–[19]. In particular, the Ellipsoidal-statistical (ES)-FP model devised [20] and was compared with the cubic-FP model [21]. The comparison suggests that the former gives more accurate shock profiles, while the latter provides a better heat-transport prediction at lower Knudsen number regimes.

There are hybrid particle methods for treating hypersonic continuum-rarefied flows [22]. Recently, hybrid Fokker-Planck-DSMC method was developed to reduce computational costs of simulations [23]. Jenny et al. [24] analyzed the bias error of the FP method for rarefied gas. As an effective means to reduce it, exponentially weighted time averaging was explored. They demonstrated how the error could be reduced without increasing the particle number for a uniform shear flow.

Although there are some published works on the FP approach, there is still a requirement for a detailed study focusing on the accuracy and efficiency of the method. In this paper, one dimensional Couette and two-dimensional cavity flow are considered over a broad range of Knudsen numbers ranging from the slip flow regime up to free molecular one. The border of the accuracy of the FP scheme is clearly determined and connected to the specific flow characteristics. In addition, a CPU-time investigation is reported, which compares the advantages of the FP compared to the DSMC in a broad set of Kn and lid velocity. Moreover, a thermal investigation is performed in the cavity flow to detect heat lines direction and cold to hot heat transfer.

2. Fokker Planck approximation of the Boltzmann equation

Consider the Boltzmann equation as described below:

$$\left(\frac{\delta F}{\delta t}\right)_{\text{coll}} = \frac{1}{m} \int_{R^3} \int_0^{4\pi} (F(V^*)F(V_1^*) - F(V)F(V_1)) g \sigma(\Omega, g) d\Omega d^3V_1 \quad (2)$$

, where F is the mass distribution function of the particle velocity, velocities (V^*, V_1^*) are the post-collision velocities of particles, the velocities (V, V_1) are the pre-collision velocities of the particle, σ is the collision cross-section, Ω is the angle between the velocities before and after the

collision and g is the relative velocity ($g = V - V_1$). If the Kn is not too large, the temporal derivative of F can be approximated by the FP equation [8], [17], [25].

$$\left(\frac{\delta F}{\delta t}\right)_{\text{coll}} \approx -\frac{\delta}{\delta V_i}(A_i F) + \frac{1}{2}\frac{\delta^2}{\delta V_i \delta V_j}(D^2 F) = S^{FP} \quad (3)$$

, where A_i and D represent the drift and diffusion terms. Assuming the Maxwellian molecular model, second and third-order moments, which are the stress tensor and the thermal flux vector, are obtained from the Boltzmann equation.

$$P_{ij} = \int_{R^3} v'_i v'_j S^{\text{Boltz}} d^3V \quad (4)$$

$$P_i = \frac{1}{2} \int_{R^3} v'_i v'_j v'_j S^{\text{Boltz}} d^3V \quad (5)$$

, where $v' = V - U$, S^{Boltz} is the left-hand side of the Boltzmann equation and U is the cell average velocity. Assuming the Maxwellian molecular model, it can be written [8], [17], [25]:

$$P_{ij} = \frac{\delta \pi_{ij}}{\delta t} = -\frac{P}{\mu} \pi_{ij} \quad (6)$$

$$P_i = \frac{\delta q_i}{\delta t} = -\frac{2P}{3\mu} q_i \quad (7)$$

, here μ is the dynamic viscosity coefficient, P is gas pressure, π_{ij} is stress tensor, and q_i is thermal flux. As a result, the ratio between the stress and thermal flux, which represents the Prandtl number, reaches $2/3$, which is the correct value of the Prandtl number for single-atomic gases [9].

By applying the same method to the S^{FP} operator and assuming the scalar diffusion coefficient and

that $\int_{R^3} (A_i v'_j + A_j v'_i + D^2 \delta_{ij}) F d^3V$ is trace free, it can be written:

$$P_{ij} = \int_{R^3} (A_i v'_j + A_j v'_i + D^2 \delta_{ij}) F d^3V \quad (8)$$

$$P_i = \int_{R^3} (A_i v'_j v'_j + 2A_j v'_j v'_i) F d^3V \quad (9)$$

, where δ_{ij} is the Dirac delta.

2.1. Fokker Planck approximation coefficients

It is crucial to find an appropriate formula for the coefficients A and D . The simplest form of the equation is a quadratic equation, but it can divert the solution [26]. For the drift coefficient, a polynomial function of the fluctuating velocity was presented by Gorji [14], which provides a good match for the viscosity and the Prandtl number. In this work, the fourth-order model introduced by Gorji and Jenny is used [14].

$$A_i = \tilde{C}_{ij}v'_j + \gamma_i \left(v'_j v'_j - \frac{3kT}{m} \right) + \Lambda \left(v'_i v'_k v'_k - \frac{2q_i}{\rho} \right) \quad (10)$$

Here, the symmetric tensor \tilde{C}_{ij} , the γ_i vector and the numerical value of Λ will be determined later. Assuming $\Lambda = 0$, $\gamma_i = 0$ and $\tilde{C}_{ij} = (-\delta_{ij})/\tau$, a simple Langevin linear equation is achieved, which leads to the wrong Prandtl number ($Pr = \frac{3}{2}$). At first, the numerical value Λ was considered as below:

$$\Lambda = -\frac{1}{\alpha\rho^3} |\det(\pi_{ij})| \quad (11)$$

, where $\det(\pi_{ij})$ is the determinant of the stress tensor π_{ij} and $\alpha = \tau(3kT)/4m$ is a scaling factor with $\tau = 2\mu/P$ the relaxation time.

To close the system of equations, a diffusion coefficient must be selected. According to the simple Lagrange equation, the diffusion coefficient is considered as below:

$$D = \sqrt{\frac{4e_s}{3\tau}} \quad (12)$$

, where e_s is the internal energy of particles. As a result, the FP equation approximation of the Boltzmann equation for single atomic gas was derived as follows:

$$\begin{aligned} \frac{\delta F}{\delta t} + V_i \frac{\delta F}{\delta x_i} + G_i \frac{\delta F}{\delta V_i} + \frac{\delta}{\delta x_i} \left(\tilde{c}_{ij} v'_j + \gamma_i \left(v'_j v'_j - \frac{3kT}{m} \right) + \Lambda \left(v'_i v'_k v'_k - \frac{2q_i}{\rho} \right) \right) F \\ = \frac{\delta^2}{\delta V_i \delta V_j} \left(\frac{kT}{m\tau} F \right) \end{aligned} \quad (13)$$

The coefficients c_{ij} and γ_i must be obtained by solving linear equations. The following equations are obtained by comparing Eq. (6) with Eq. (8) for stress tensor and Eq. (7) with Eq. (9) for thermal flux.

$$c_{il} p_{jl} + c_{jl} p_{il} + 2\gamma_i q_j + 2\gamma_j q_i + 2\rho \Lambda \langle M'_i M'_j M'_k M'_k \rangle = 0 \quad (14)$$

$$\begin{aligned} 4\Lambda \left[\langle M'_i M'_j M'_j M'_i \rangle - \frac{q_i p_{il}}{\rho^2} - \frac{3kT q_i}{m\rho} \right] + 2C_{jl} \langle M'_i M'_j M'_i \rangle + 2C_{il} \frac{q_l}{\rho} \\ + 2\gamma_i \left[\langle M'_i M'_i M'_i M'_j \rangle - \frac{3kT p_{ij}}{m\rho} \right] + \gamma_i \left[\langle M'_i M'_i M'_j M'_j \rangle - 9 \left(\frac{kT}{m} \right)^2 \right] = -\frac{10q_i}{3\rho\tau} \end{aligned} \quad (15)$$

, while $M' = M - U$ and M is the particle velocity. Although simplifications have been made to derive the FP equation, still the complexity of the solution domain makes the direct simulation of Equation (14) and (15) rather expensive. To cope with that, these equations were transformed into the equivalent Ito processes [5].

$$dM_i = A_i dt + G_i dt + D dW_i \quad (16)$$

$$dX_i = M_i dt \quad (17)$$

, where dW_i are independent Wiener increments with zero expectation and variance dt . Equations (16) and (17) have many numerical advantages in small and medium Knudsen numbers. Also, in contrast to the DSMC, the collision between particles is not calculated, which is a process that is associated with a high computational cost in small Knudsen numbers.

Since Equations (16) and (17) form a nonlinear stochastic system, one cannot find an analytic solution such as the Langevin linear model. For simplicity, it is assumed that there is no external force ($G_i = 0$). The solution strategy is to divide the nonlinear Equation (16) into a Langevin linear part L and a nonlinear remainder part N :

$$dM_i = -\frac{1}{T}M'_i dt + DdW_i + C_{ij}M'_j dt + Y_i(M'_j M'_j - \langle M'_j M'_j \rangle)dt + \Lambda(M'_i M'_k M'_k - \langle M'_i M'_k M'_k \rangle)dt \quad (18)$$

First, the linear part, $dM_i = dL_i$, is considered, and for a nonlinear part, a first-order forward Euler time integration scheme is employed. At first, the velocity is inspected with the linear model:

$$dM_i = \frac{-1}{\tau} (M_i(t) - U_i(x(t), \tau))dt + G_i(x(t))dt + \sqrt{\frac{kT(x(t), \tau)}{m\tau(x(t), \tau)}} dW_i \quad (19)$$

For simplicity, the dependencies of the parameters are not considered relative to the location of the particles $x(t)$. To calculate the mean velocity, the following relation is established:

$$U_i(t^{n+1}) = U_i(t^n) + G_i \Delta t \quad (20)$$

By introducing the fluctuating velocities $M(t) = M'(t) - U(x, t)$, it can be written:

$$dM'_i(t) = -\frac{1}{T}M'_i(t) + \sqrt{\frac{2kT}{m\tau}} dW_i \quad (21)$$

There is an analytical solution for the differential equation above:

$$M'_i(t^{n+1}) = M'_i(t^n)e^{-\frac{\Delta t}{T}} + \sqrt{\frac{kT}{m\tau}} \left(1 - e^{-\frac{2\Delta t}{T}}\right) \xi_i \quad (22)$$

, where ξ_i is the independent variable; thus, by combining Equations (20) and (22), the final relation is obtained for a linear model similar to reference [27].

$$M_i^{n+1} = M_i^n e^{-\frac{\Delta t}{T}} + U_i^n \left(1 - e^{-\frac{\Delta t}{T}}\right) G_i \Delta t + \sqrt{\frac{kT}{m\tau}} \left(1 - e^{-\frac{2\Delta t}{T}}\right) \varepsilon_i \quad (23)$$

The expression of the fourth-order drift was divided into a linear part and its remainder. Regarding the linear solution and adding the solution of the nonlinear part, it can be written:

$$M_i(t^{n+1}) = M_i(t^n)e^{-\frac{\Delta t}{\tau}} + U_i^n \left(1 - e^{-\frac{\Delta t}{\tau}}\right) G_i \Delta t + \sqrt{\frac{kT}{m\tau} \left(1 - e^{-\frac{2\Delta t}{\tau}}\right)} \xi_i + e^{-\frac{\Delta t}{\tau}} \int_0^{\Delta t} e^{\frac{t}{\tau}} N_i dt \quad (24)$$

$$N_i = C_{ij}M_j' + Y_i \left(M_j' M_j' - \frac{3kT}{m}\right) + \Lambda \left(M_i' M_j' M_i' - \frac{2q_i}{\rho}\right) \quad (25)$$

By implementing simplifications in Equation (24), the following equation can be obtained [9]:

$$M_i^{n+1} = \frac{1}{\alpha} \left(M_i^n e^{-\frac{\Delta t}{\tau}} + \left(1 - e^{-\frac{\Delta t}{\tau}}\right) \tau N_i^n + \sqrt{\frac{kT}{m\tau} \left(1 - e^{-\frac{2\Delta t}{\tau}}\right)} \xi_i \right) + U_i^n + G_i \Delta t \quad (26)$$

$$\alpha^2 = 1 + \frac{m\tau}{3kT} (\tau(1 - A)^2 \langle N_i^n M_i^n \rangle + 2(A - A^2) \langle N_i^n M_i^n \rangle) \quad (27)$$

$$A = e^{-\frac{\Delta t}{\tau}}$$

Using a precise solution to solve the linear part and approximations performed for solving the nonlinear part, like the particle velocity, a plan for the exact position of the particle can be derived [8].

2.2. FP Algorithm Outline

To start simulations, a specific number of particles (np) with the weight of w_i is generated based on the distribution function $F(V, x, t)$. It should be noted that the time step is determined according to the Courant number. The FP algorithm at each time step is depicted in Figure 1. Although this algorithm is similar to the DSMC, the molecular collision part in the DSMC method is replaced with Eq. (26). Couette flow and cavity flow are used in this paper as simple one-dimensional and two-dimensional flows. The researchers in Roohi's group already evaluated these flows over a wide range of Knudsen numbers using DSMC [28]–[33]. By replacing a set of FP moment calculations with the DSMC collision part, the FP solver was obtained.

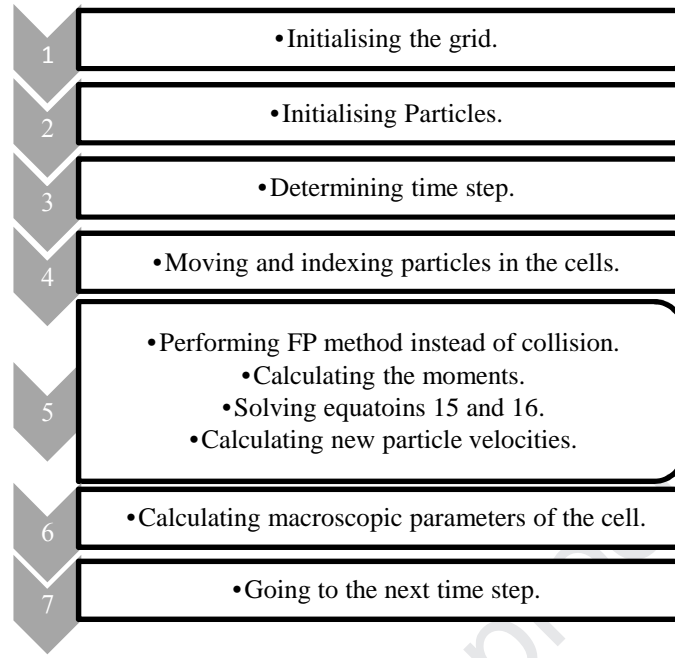


Fig. 1 The FP algorithm

3. Couette Flow

As a one-dimensional flow; Couette flow is a well-known flow for studying gas behavior in non-equilibrium conditions. Figure 2 (a) shows the schematic of the Couette flow. As it is shown, the walls are at the same temperature ($T_1=T_2$) and the same velocity magnitude but different directions.

4. Cavity Flow

As the second case, cavity flow is considered to simulate rarefied two-dimensional flow at non-equilibrium conditions. A schematic of the micro/nano cavity is presented in Figure 2 (b). The cavity lid moves in the positive direction of the horizontal axis with U_w . By applying different Kn and wall velocities in the domain, the cavity flow experiences different rarefaction regimes. The temperature of the walls is considered constant and equal to T_w . The cavity flow behavior was investigated using the FP method at different Knudsen numbers and flow velocities. The results were compared with DSMC solutions.

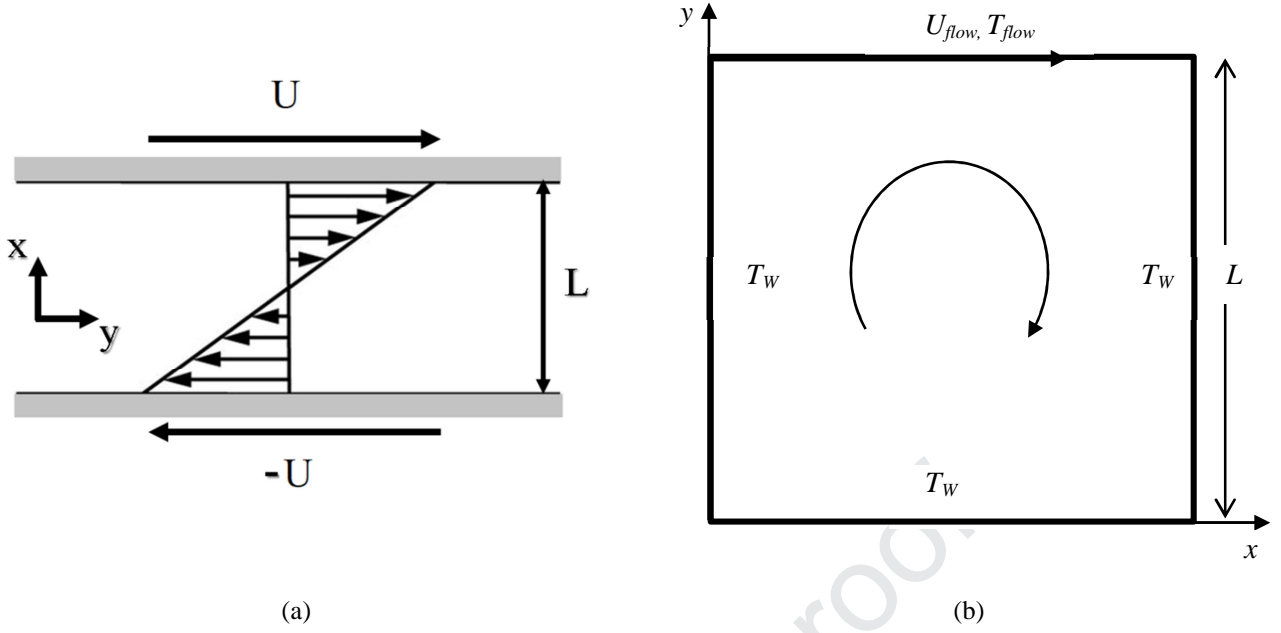


Fig. 2 Schematic of the a) Couette flow and b) Cavity flow

5. Results and discussion

5.1. Couette flow

At first, argon gas in the Couette flow is investigated. Gas molecules are considered as Maxwellian molecules with a viscosity power index of 1. The walls move in the opposite direction with a speed magnitude of $U_w = 50 \text{ m/s}$ ($Ma=0.16$), and both walls are considered diffusive reflector with a temperature of $T_w=273.15 \text{ K}$, and a reference temperature $T_{ref} = 273.15 \text{ K}$. In this case, the value of the Kn varies between 0.005 and 0.3. The distance between the two plates is set $L = 0.001 \text{ m}$. The molecular mass of argon gas is equal to $6.63 \times 10^{-26} \text{ Kg}$ and its molecular diameter is $4.17 \times 10^{-10} \text{ m}$. 200 cells are chosen for the simulation.

Three various particles per cell (PPC), i.e., 500, 1000 and 1500 were selected to study the independence of the numerical solution from the number of particles. The results for velocity and temperature are shown in Figure 3. As shown, the velocity profile (Figure 3 (a)) matches well to the results of the DSMC at different PPCs. However, there is a little difference between the DSMC and FP in the temperature profile (Figure 3 (b)). It should also be noted that this temperature difference

is ignorable in comparison with the entire range of temperature variations (about 0.2 degrees Kelvin at maximum). For the rest of simulations, 100 cells and 1000 particles in each cell were selected.

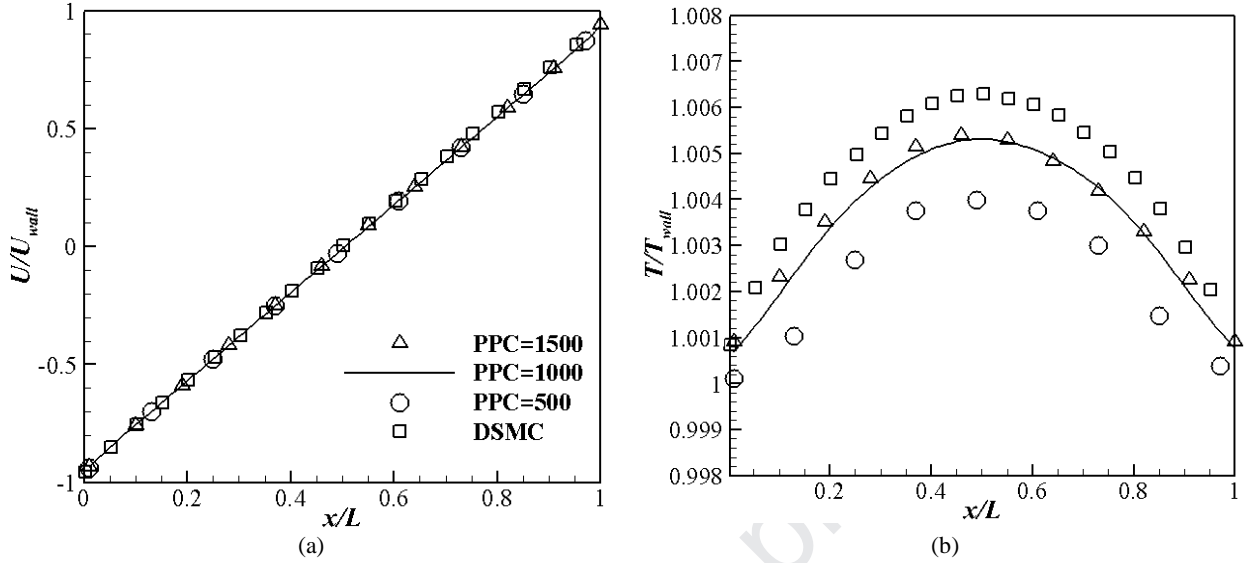


Fig. 3 PPC study at $U_w=50$ m/s a) Velocity b) Temperature profiles.

Figure 4 (a-d) shows the profile of the non-dimensional velocity, temperature, shear stress and heat flux over a wide range of Knudsen numbers. It is noteworthy that in the Couette geometry at very low Knudsen numbers, the velocity profile is almost linear; however, as shown in Figure 4 (a), by increasing Kn, the velocity profile adjacent to the walls becomes nonlinear due to the growth of the Knudsen layer. Moreover, the gas velocity near the walls deviates from the wall velocity due to non-equilibrium effects. The FP method presents a suitable agreement with the DSMC in the investigated Kn range. As Kn increases, the accuracy of the FP results begins to decrease. As shown in Figure 4 (a) for $Kn = 0.3$, there is a slight deviation from DSMC results in the velocity profile of the FP near the walls.

As it is observed in Figures 4 (a) & (b), FP has captured temperature and velocity jump and the Knudsen layer near the wall accurately. Moreover, according to Figure 4 (c) & (d), the FP method shows suitable predictions for shear stress and heat flux in low Knudsen numbers compared to DSMC. However, at high Knudsen numbers, the results show more deviation from DSMC.

In order to compare DSMC and FP in more detail, the relative error is defined as follows:

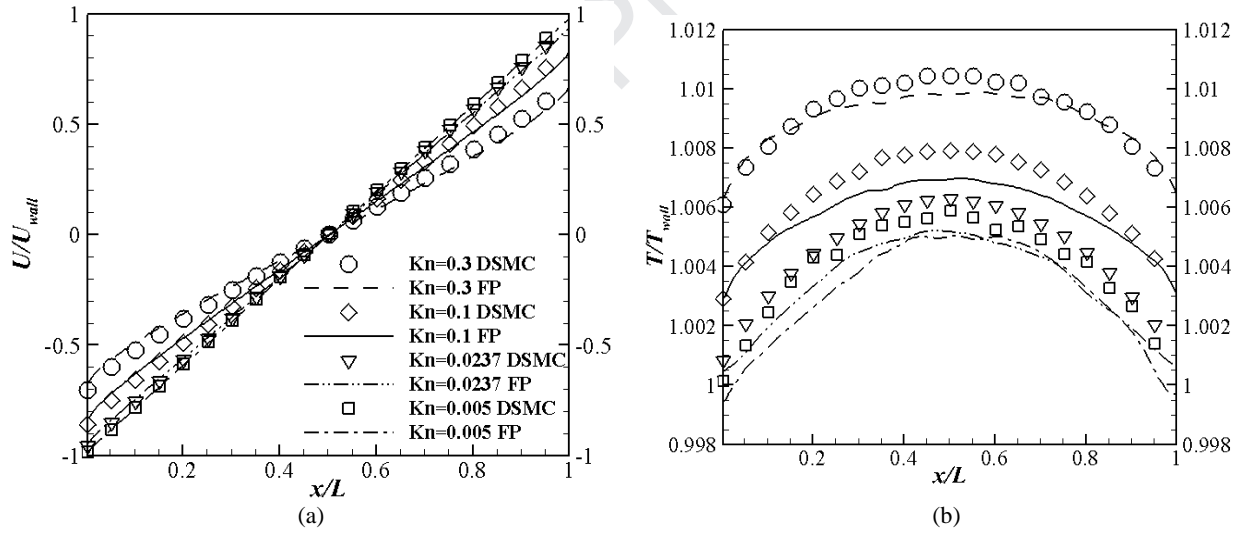
$$Error = \frac{|a_{FP}| - |a_{DSMC}|}{|a_{ref}|} \quad (28)$$

, where a is a macroscopic feature such as velocity, temperature, shear stress and heat flux. The subscript ref indicates the reference value of parameter a that could be wall velocity, wall temperature, reference pressure (P_0) and reference heat flux q_0 , P_0 and q_0 are defined as below:

$$q_0 = 0.5\rho_\infty U_{wall}^3 \quad (29)$$

$$P_0 = \rho_\infty \frac{kT_{ref}}{m} \quad (30)$$

The maximum relative error is about 4% of U_w for velocity, about 0.1% of T_w for temperature, 0.8% of P_0 for shear stress and 9% of q_0 for heat flux.



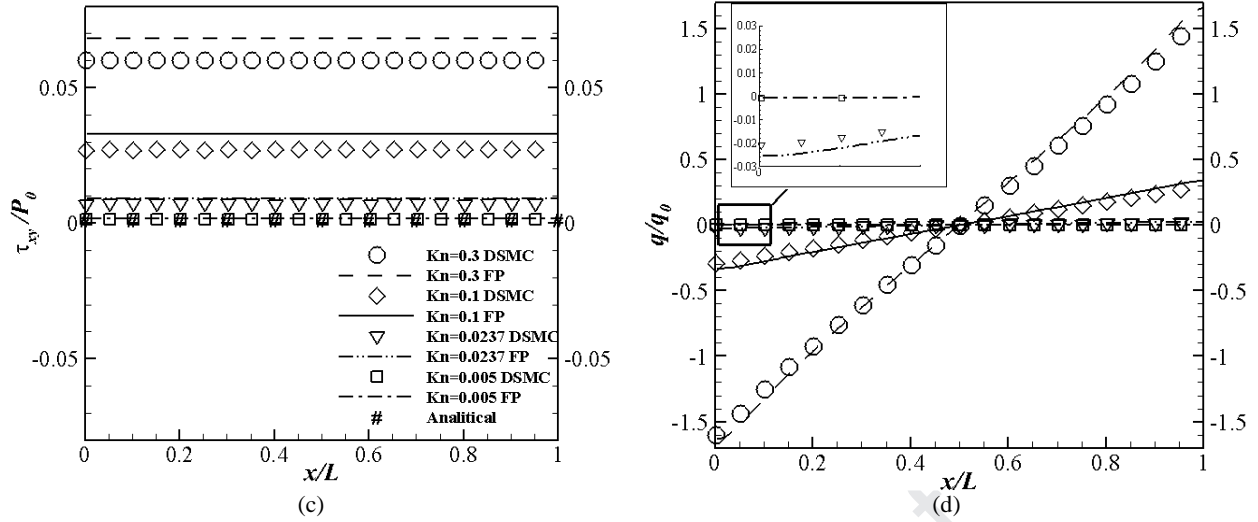


Fig. 4 Investigation of the Kn effects in the Couette flow with $U_w=50$ m/s, a) Velocity b) Temperature c) Shear stress d) Heat flux

As the second case, Couette flow at a wall speed of $U_w=1000$ m/s ($Ma=3.1$) is considered. Both wall temperature and the reference temperature are set equal to $T_w = T_{ref} = 300$ K. Various PPCs, i.e. 40, 50, 100, 150 and 200 are selected for studying PPC independence. As shown in Figure 5 (a), the velocity profiles are in good agreement at different PPCs. Note that the velocity profile is a first-order moment; therefore, the influence of PPC is negligible. However, a second-order moment like temperature, Figure 5 (b), depicts the difference between 40 to 200 PPC solutions. Thus, PPC=150 was chosen for the rest of the simulations reported for the Couette flow.

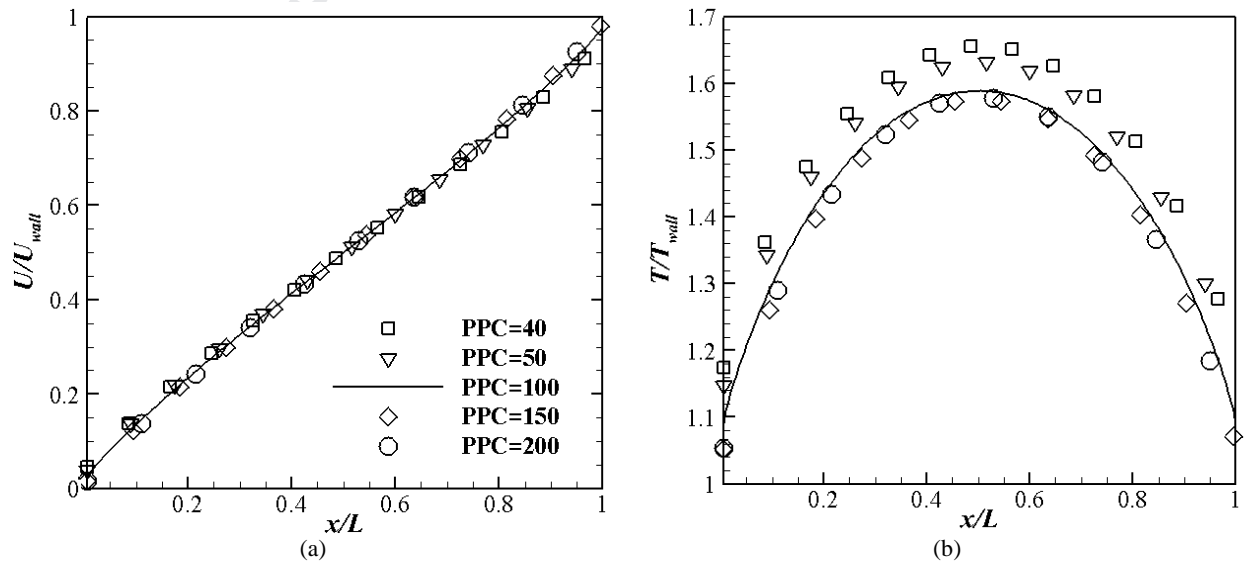
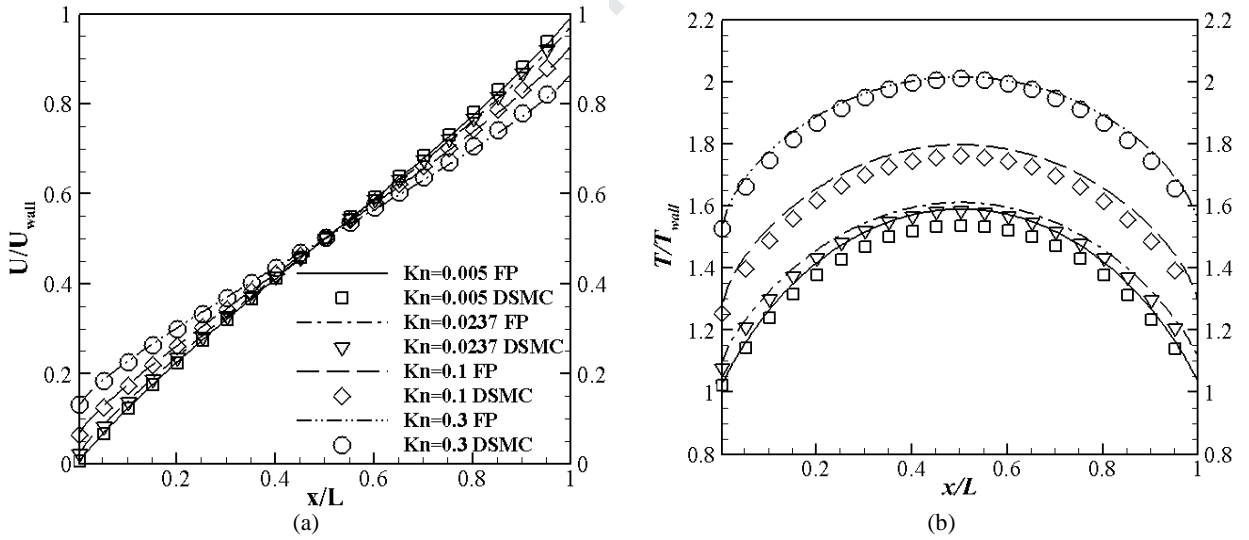


Fig. 5 PPC study at $U_w=1000$ m/s a) Velocity b) Temperature

Figures 6 (a-d) show the distribution of non-dimensional velocity, temperature, shear stress and heat flux. It is observed that the FP method provides precise results for a wide range of Knudsen numbers in the supersonic flow regime. As shown in Figure 6 (a), the velocity magnitudes correspond well to DSMC. By comparing Figures 4 and 6, it can be concluded that the accuracy of the FP method increases by increasing the Mach number. Additionally, these Figures prove that decreasing the Kn cause more precise results for FP. The maximum relative error is about 0.4% of U_w for speed, about 5% of T_w for temperature, 8% of P_0 for shear stress and 0.3% of q_0 for heat flux.

Similar to subsonic Couette flow, there are velocity and temperature jumps in supersonic flow. Figure 6 (a) and (b) state that at high Kn, the velocity profile becomes nonlinear near the walls and the magnitude of the temperature jump becomes considerable and raised up to 50% greater than the wall temperature.



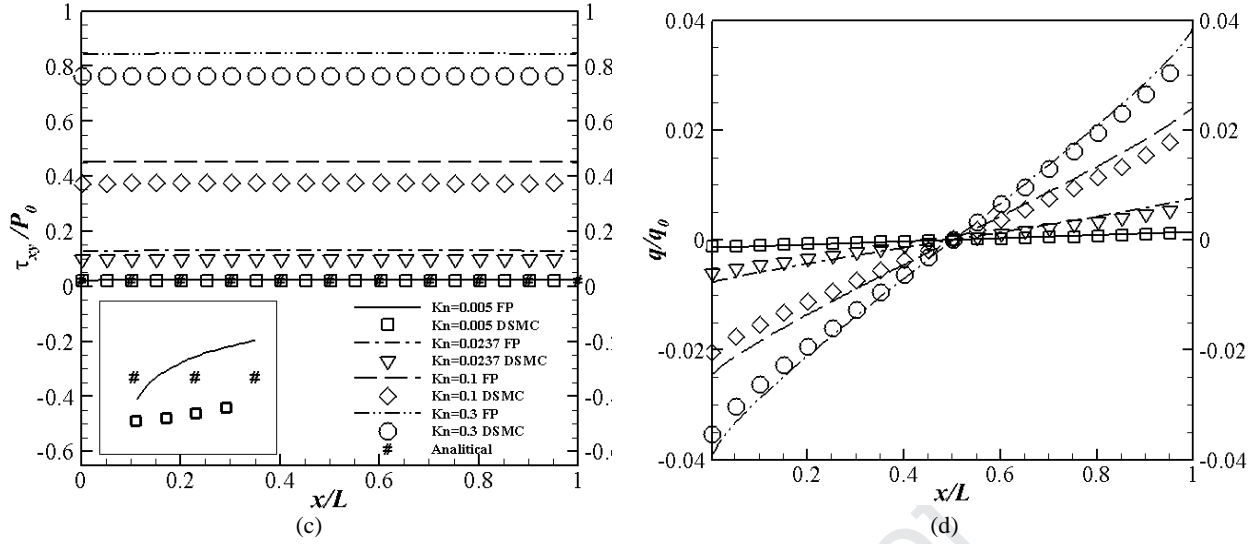


Fig. 6 Kn dependence investigation of the Couette flow with $U_w=1000$ m/s
a) Velocity b) Temperature c) Shear stress d) Heat flux

In the following, a convergence study was carried out for FP results in the Couette flow. The convergence criterion is considered as follow:

$$convergence_index(a) = \frac{\sum |a^{n+1} - a^n|}{a_{ref}} \quad (31)$$

, where a is a macroscopic independent flow parameter, a_{ref} is the reference parameter of the flow and n is the time step counter. As a third-order moment of peculiar velocity, heat flux convergences slower than the other parameters. Therefore, it is selected as the parameter a , and the results are shown in Figure 7. As it is shown, the heat flux convergence is almost independent of Kn; while the convergence index increases slightly by increasing Kn.

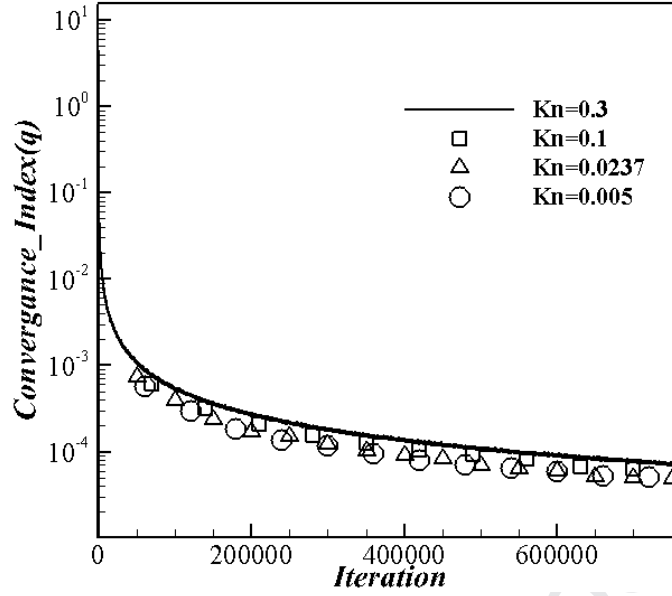


Fig. 7 Heat flux error convergence for various Knudsen numbers at $U_w=1000$ m/s.

5.2. Computational cost

In this section, the computational cost is reported. The required time of DSMC and FP algorithm was calculated for 3000 iterations. Besides, as the contribution of the collision segment in the DSMC and particle evolution in FP was presented in percentage (Table 1). In this case, wall velocity is considered $U_w=1000$ m/s and $Kn=0.01$. A grid with 200 cells and 150 PPC was considered for both DSMC and FP methods. Both algorithms were run on a computer with CPU of Intel® Core i7 @ 3.40GHz and 24GB of RAM. Table 1 clearly shows the advantage of the FP method, e.g., a lower computational cost of the approach in comparison with DSMC.

As shown in Table 1, the most time-consuming part in this algorithm is dedicated to collision part in DSMC and particle evolution in FP, that is 87% and 63% of total time calculations, respectively. Additionally, DSMC collision takes 3.8 longer times than FP particle evolution. The reason comes back to a larger number of selected pair for collision (N_c) in the no-time-counter (NTC) model in DSMC, that is [34]:

$$N_c = \frac{1}{2} \frac{N(N-1)F_N (\sigma_T C_r)_{\max} \Delta t}{V_c} \quad (32)$$

, where N_c is the maximum number of particle pairs checked for collision in each cell with N particles, F_N is the ratio of real gas molecules to simulated DSMC particles, $(\sigma_T C_r)_{\max}$ is the maximum of collision cross-section multiplied by relative velocity, and V_c is the cell volume. On the other hand, FP solves a system of equations corresponding to the total number of particles in the domain [9].

Although FP works faster than DSMC in particle evolution (3.8 times faster), there is a difference in the sampling procedure of the DSMC and FP [10]. Sampling in FP is more time consuming than sampling in DSMC; thus, the overall CPU-time of FP to DSMC is not as considerable as the CPU-time of collision ratio of these models.

Table 1 CPU-time study for DSMC and FP methods in the Couette flow @ $Ma=3.1$ & $Kn=0.01$

Parameter	Magnitude
<u>DSMC Collision</u>	3.8
FP Particle Evolution	
<u>DSMC Collision</u>	87 %
DSMC CPU time	
<u>FP Particle Evolution</u>	63 %
FP CPU time	
<u>DSMC CPU Time</u>	2.7
FP CPU time	

The computational cost per each particle for the FP and DSMC method is presented at different Knudsen numbers in Table 2. As it is shown, the CPU-time per each particle in the DSMC increases by decreasing Kn. Higher DSMC convergence rates at higher Mach numbers can be explained by considering the fact that the uncertainty associated with the moment estimators scales with the inverse of the Mach number in DSMC [35], while in the FP method it is independent of Kn, and it is almost constant in the investigated Kn range. The reason could be that rarefaction does not play a

role in increasing the execution time in the FP method [10]. Additionally, it is evident that FP needs less time per each particle at higher velocities. This fact completes our previous discussion about the accuracy of FP at high velocities. In other words, FP algorithm works more accurately and more efficiently at high velocities. The last column of Table 2 shows the CPU-time ratio comparison between DSMC and FP. It is clear that DSMC is faster at lower velocities and high Knudsen numbers; while approaching the continuum regime makes DSMC more expensive. Therefore, considering Figure 4 and Table 2, compared to DSMC, using the FP method for treating the Couette flow is recommended at higher wall velocities and lower Knudsen numbers. On the other hand, DSMC is better to be used at lower velocities but at higher Kn. For high velocity cases like $U_w=1000\text{m/s}$, considering Figure 6 and Table 2, using FP is advised for all Knudsen numbers because of accurate results and lower CPU-time. Recall that Table 2 also indicates that by increasing the wall velocity DSMC consumes more time per each particle. However, computational time decreases in FP. Therefore, FP works faster at higher velocities.

Table 2 CPU-time comparison between DSMC and FP methods in Couette flow

$U_w (m/s)$	Kn	$\left(\frac{\text{CPU time}}{n_p}\right)_{DSMC} (s/particle)$	$\left(\frac{\text{CPU time}}{n_p}\right)_{FP} (s/particle)$	$\frac{\text{DSMC CPU time}}{\text{FP CPU time}}$
50	0.3	5.64×10^{-5}	2.52×10^{-6}	0.45
	0.1	6.89×10^{-5}	2.67×10^{-6}	0.52
	0.0237	1.13×10^{-4}	2.63×10^{-6}	0.86
	0.005	1.38×10^{-4}	2.59×10^{-6}	1.07
1000	0.3	6.94×10^{-5}	5.11×10^{-7}	2.72
	0.1	7.12×10^{-5}	4.99×10^{-7}	2.85
	0.0237	1.16×10^{-4}	5.00×10^{-7}	4.66
	0.005	1.61×10^{-4}	5.08×10^{-7}	6.34

5.3. Cavity flow

In this section, the cavity flow is considered at two different wall velocities $U_w=100$ m/s ($Ma=0.31$) and $U_w=300$ m/s ($Ma=0.93$). The Kn range changes from 0.05 to 100. The boundary conditions are assumed to be diffusive reflector at $T_w=300$ K. The size of the cavity is considered 10^{-6} (m^2).

5.3.1. Grid-convergence and computational costs

Grid-convergence was performed for cavity case with $Kn=1$ and $U_w=300$ m/s. Different grids were selected for the grid study, i.e., 60×60 , 90×90 , 120×120 , 150×150 , 180×180 , and 200×200 . The results for the velocity and temperature profile over a line passing at $y=3L/4$ are shown in Figure 8. As Figure 8 (b) depicts, the temperature profile of the FP method is in suitable agreement with the DSMC solution almost for all the investigated grids. However, the velocity profile (Figure 8 (a)) shows a slight difference at $x=0.55L$. By comparing FP and DSMC solutions, it is observed that solutions of 150×150 , 180×180 , and 200×200 Grids are close to each other. Therefore, the 150×150 Grid seems to be adequate enough for both FP and DSMC.

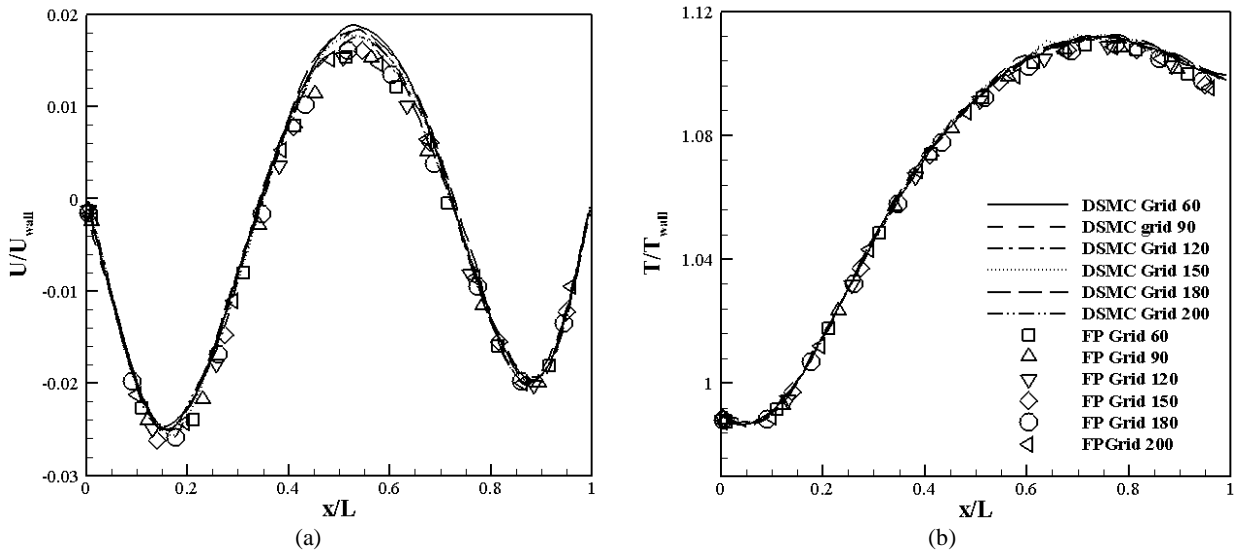


Fig. 8 Grid study for the cavity flow at $U_w=300$ m/s, $Kn=1$ a) velocity b) temperature profiles.

As a result, a grid of 150×150 computational cells and 200 PPC was considered for FP, similar to Ref. [9]. Additionally, a grid of 150×150 cells and 20 PPC was used for the DSMC similar to Ref. [28].

Table 2 shows the CPU-time comparison between different grid cases for the FP and DSMC solutions at $Kn=1$ and $U_w=300$ m/s. The CPU-time of the FP is almost three to four times faster than DSMC in all the investigated grids. In addition, CPU-time per each particle is increased by increasing the grid for DSMC.

Table 2 CPU-time comparison between DSMC and FP methods in Couette flow

U_w (m/s)	Kn	Grid	$\left(\frac{\text{CPU time}}{n_p}\right)_{DSMC}$ (s/particle)	$\left(\frac{\text{CPU time}}{n_p}\right)_{FP}$ (s/particle)	$\frac{\text{DSMC CPU time}}{\text{FP CPU time}}$
300	1	60×60	7.71×10^{-5}	2.19×10^{-6}	3.53
		90×90	8.91×10^{-5}	2.31×10^{-6}	3.87
		120×120	9.61×10^{-5}	2.38×10^{-6}	4.04
		150×150	1.22×10^{-4}	3.19×10^{-6}	3.84
		180×180	1.07×10^{-4}	2.92×10^{-6}	3.68
		200×200	1.16×10^{-4}	3.11×10^{-6}	3.74

To evaluate the accuracy of the results of the FP method, the velocity, temperature, shear stress, and heat flux were compared with the DSMC results at $y=3L/4$. The results were depicted in Figure 9 (a, c, e, g) for $Kn \leq 0.2$ and (b, d, f, h) for $Kn > 0.2$. As it is shown in Figure 9, the FP solution becomes more consistent with the DSMC by increasing Kn .

Figure 9 (a-b) shows that by increasing the Kn , the velocity decreases first due to the increase of viscous effects in the flow. As shown in Figure 9 (c-d), at high Kn , temperature deviates from the wall temperature near the walls of the cavity, i.e., temperature jump effects. The increase of temperature jump at higher Kn is because of increasing the non-equilibrium effects in the transition and free molecular regimes, which can be explained by the change in the rate of intermolecular

collisions. Intermolecular collisions happen less frequently in a non-equilibrium state. Thus, particles sense the effect of walls less than a near-equilibrium condition [4].

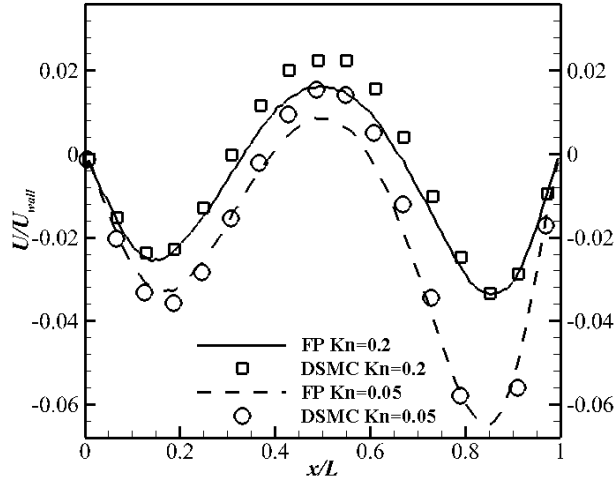
In Figure 9 (e-f), shear stress τ_{xy} is non-dimensionalized with respect to τ_0 , that is:

$$\tau_0 = 0.5\rho_\infty U_{wall}^2 \quad (33)$$

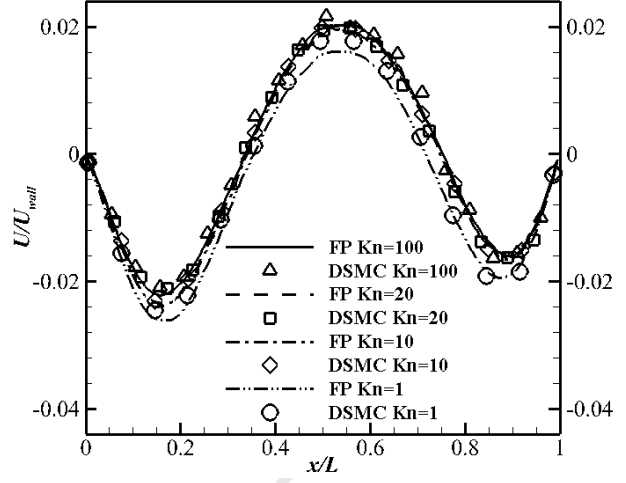
, where ρ_∞ is the initial density at the corresponding Kn.

From the molecular point of view, the magnitude of shear stress can be determined by the frequency and correlation of molecular velocities. By dividing the shear stress by the initial density of the gas, the rarefaction effects on reducing the shear stress are eliminated [30]. Therefore, Figure 9 (e-f) shows the ratio of collision rate and correlation to the existing number of particles. By increasing the Kn, particles experience less intermolecular collisions, as a result, particles conserve their energy for the potential collisions. Thus, shear stress increases at higher Kn. Figure 9 (e-f) also shows that by increasing the Kn the inter-molecular collisions occur in the right region more than the left region of the cavity, while in lower Kn, the equilibrium conditions lead to a symmetric distribution of shear stress in the cavity. As shown in Figure 9 (g-h), by increasing the Kn, heat transfer variation in the right wall is more considerable than the left wall. There are more molecular interactions at the right side due to a higher density of the gas there; thus, it is more affected by Kn than the left side.

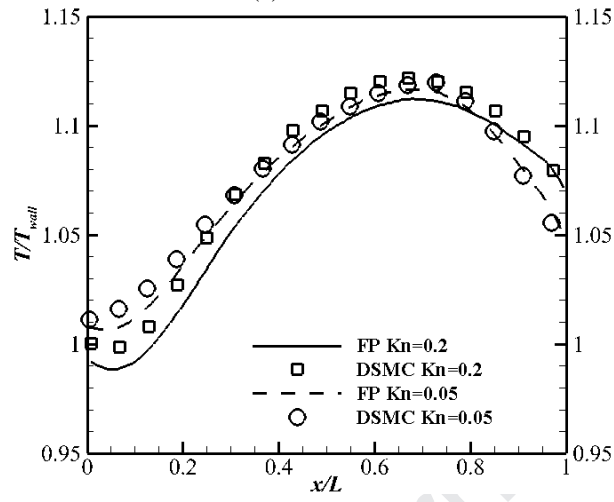
The maximum relative error in different cases is around 0.7% of U_w in velocity profile (Figure 9 (a)) at Kn=0.05 and occurs at $x=0.55L$.



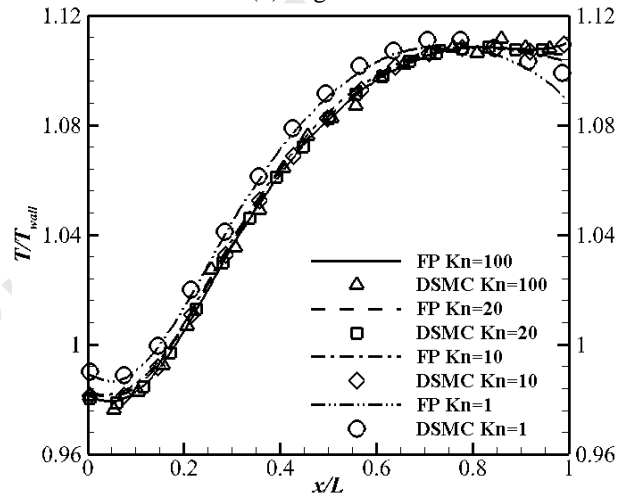
(a) Low Kn



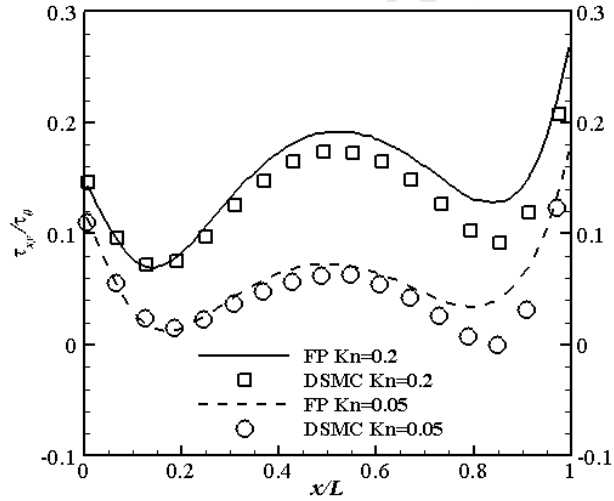
(b) High Kn



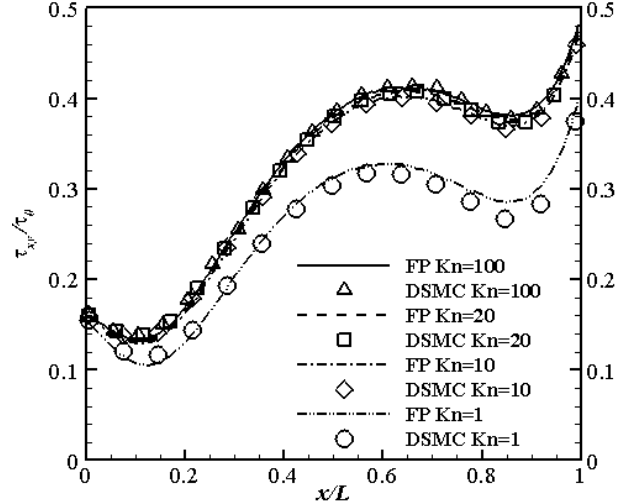
(c) Low Kn



(d) High Kn



(e) Low Kn



(f) High Kn

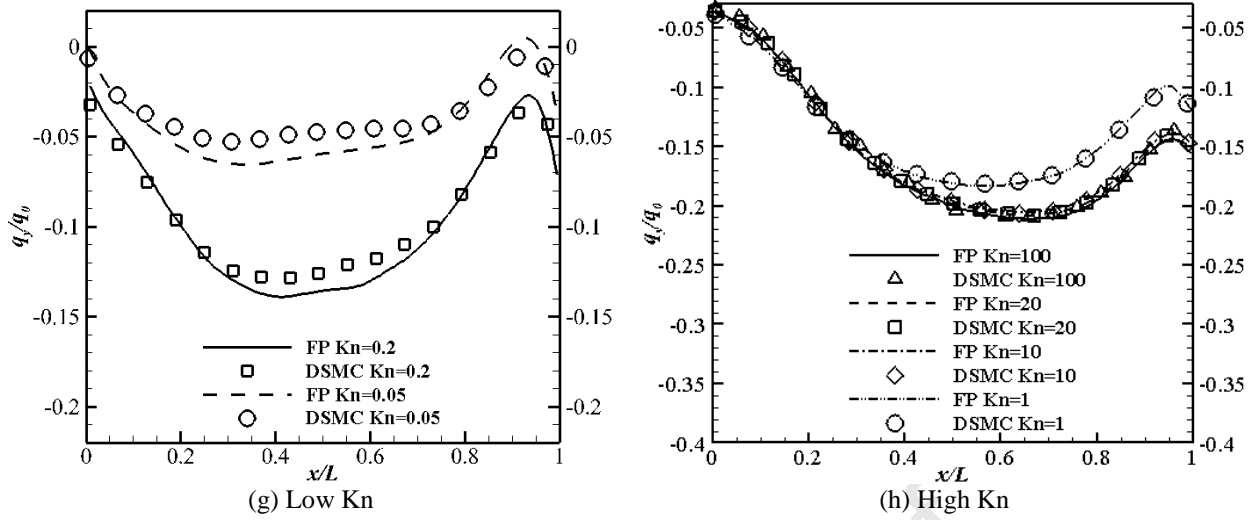


Fig. 9 Various profiles at different Kn at $y=3L/4$ for the cavity with $U_w=300$ m/s:
a-b) Velocity c-d) Temperature e-f) Shear stress g-h) Heat flux

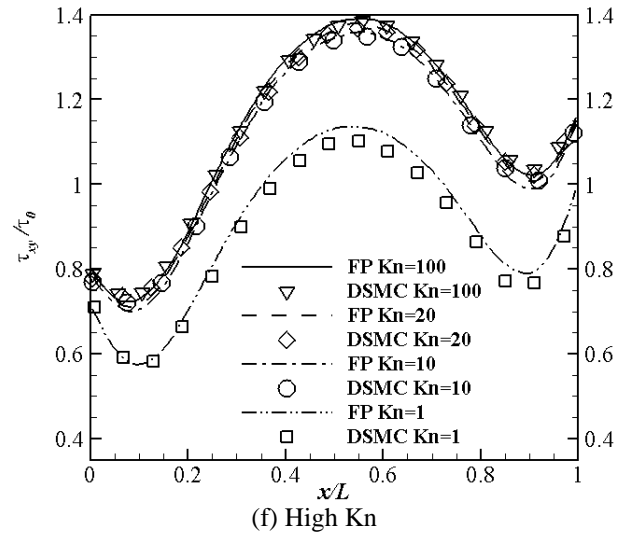
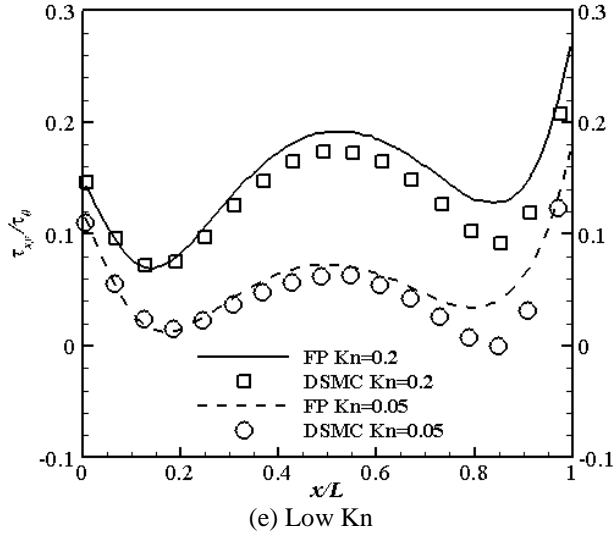
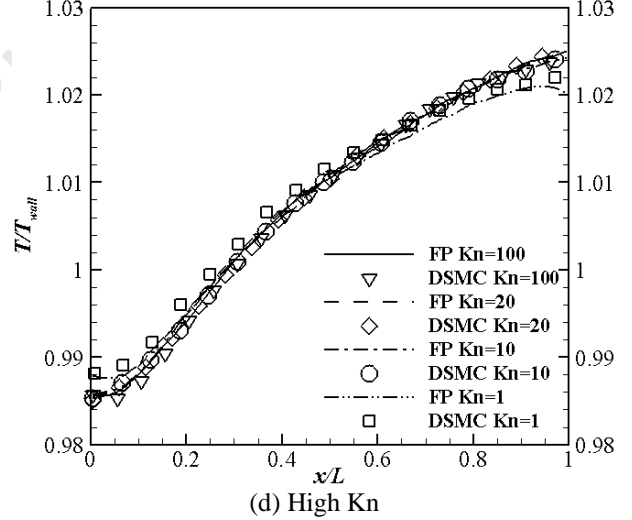
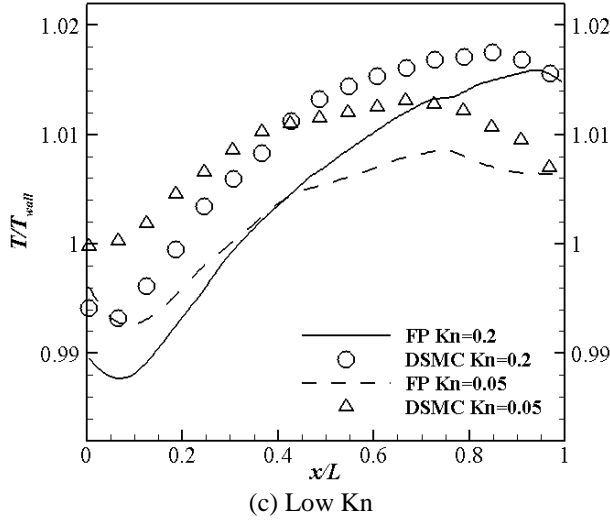
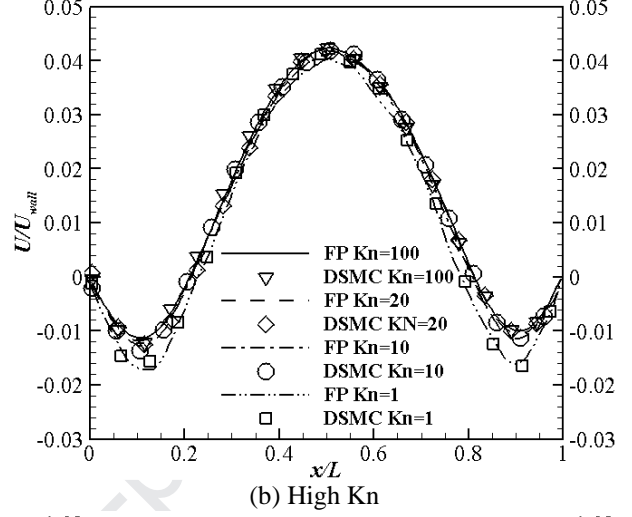
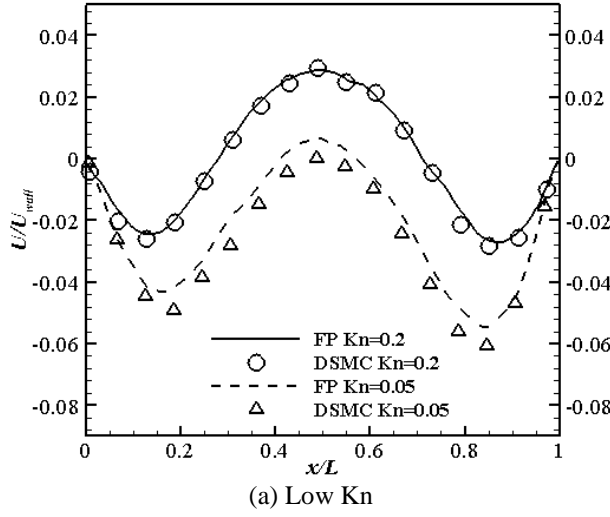
As the second case, the wall velocity of the cavity was increased to 100 m/s. The results are displayed in Figure 10 (a-h) for velocity, temperature, shear stress and heat flux in line of $y=3L/4$. As it is shown in these figures, a comparison between different Kn ranging from 0.05 to 100 is reported. Similar to the previous case, it is observed that the accuracy of the FP method increases by increasing Kn . Comparing Figures 9 and 10, it is concluded that the FP method works better at higher lid velocities in cavity case.

Figures 9 (a-b) and 10 (a-b) show that by decreasing the lid velocity, velocity profile distribution becomes more symmetric. It also shows that non-dimensional velocity variation is higher at lower lid velocities.

By comparing Figure 10 (c-d) and Figure 9 (c-d), it is evident that the temperature profile, as well as temperature jump, increase by increasing wall velocity at the entire Kn range.

Figure 9 (e-f) and 10 (e-f) show that by decreasing the wall velocity, the non-dimensional shear stress increases. It is shown that in lower velocities non-dimensional shear stress near the right and the left wall deviates more than higher velocities. As shown in Figure 9 (g-h) and 10 (g-h), the variation in the distribution of non-dimensional heat flux is more considerable at lower velocities.

The maximum relative error between FP and DSMC in different cases is about 0.7% of U_w in velocity profile (Figure 10 (a)) at $Kn=0.05$ occurring at $x=0.55L$.



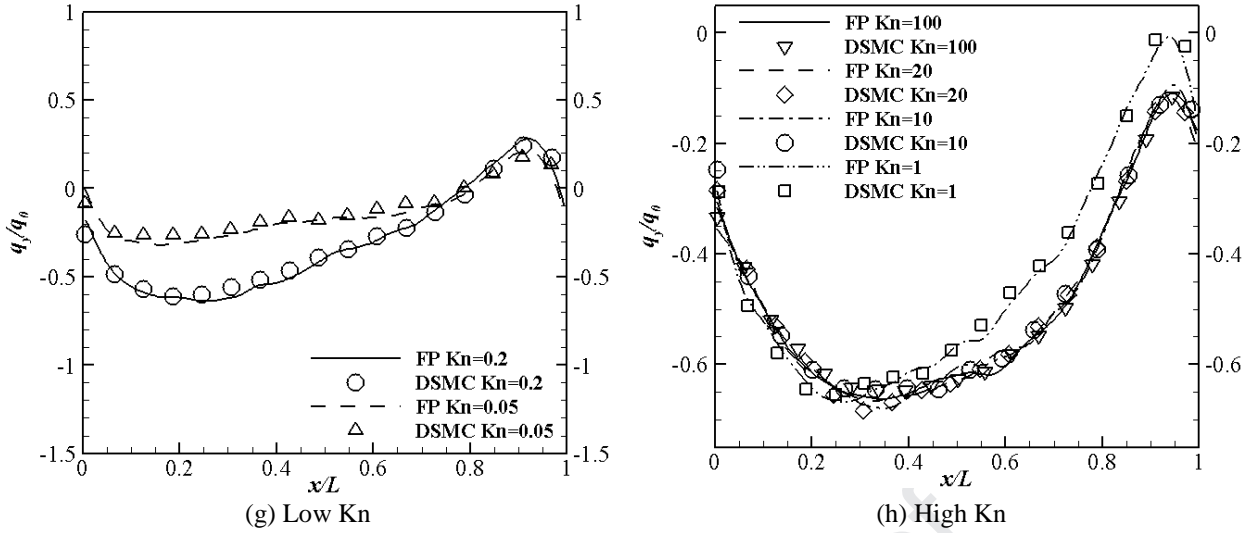


Fig. 10 Various profiles at different Kn at $y=3L/4$ for the cavity with $U_w=100$ m/s:
a-b) Velocity c-d) Temperature e-f) Shear stress g-h) Heat flux

As it shows in both cases, the maximum error happens at around $x=0.55L$ for velocity. Our investigation shows that the existence of a velocity vortex in the center of the cavity causes the most non-equilibrium effects, which lead to the maximum deviation of FP from DSMC. The parameter which expresses deviation from the equilibrium effect is gradient length Knudsen number, Kn_{GL} , which can be defined as [36]:

$$Kn_{GL\phi} = \frac{\lambda}{\phi} |\nabla\phi| \quad (34)$$

$$Kn_{GL} = \text{Max}(Kn_{GLU}, Kn_{GLT}, Kn_{GLP}) \quad (35)$$

, where ϕ is an arbitrary flow parameter.

Figure 11 shows the ratio of gradient length Knudsen number to the Knudsen number, that is $\frac{Kn_{GL}}{Kn}$, over the line $y=3/4L$ of the cavity. As it is shown at $x=0.55L$, $\frac{Kn_{GL}}{Kn}$ increases suddenly. It can be seen that by increasing the Kn, $\frac{Kn_{GL}}{Kn}$ decreases at $x=0.55L$. The reason is that local non-equilibrium effects (Kn_{GL}) increase less than global non-equilibrium effects (Kn). This means that the gas flow becomes more uniform by increasing Kn, i.e., rarefaction effects diminishes flow gradients. Additionally, Figure 11 Proves that at high Knudsen numbers ($Kn>10$), local Kn changes

proper to the global Kn. Therefore, the variation of the $\frac{Kn_{GL}}{Kn}$ becomes constant in different Kn at $x = 0.55L$. A similar result is observed in figure 9 (a), (b) and 10 (a), (b), where the maximum deviation of the FP solution from the DSMC occurs at $x = 0.55L$. Therefore, increasing $\frac{Kn_{GL}}{Kn}$ creates more local non-equilibrium effects which means $\frac{Kn_{GL}}{Kn}$ is as crucial as Kn to consider the accuracy of the solver.

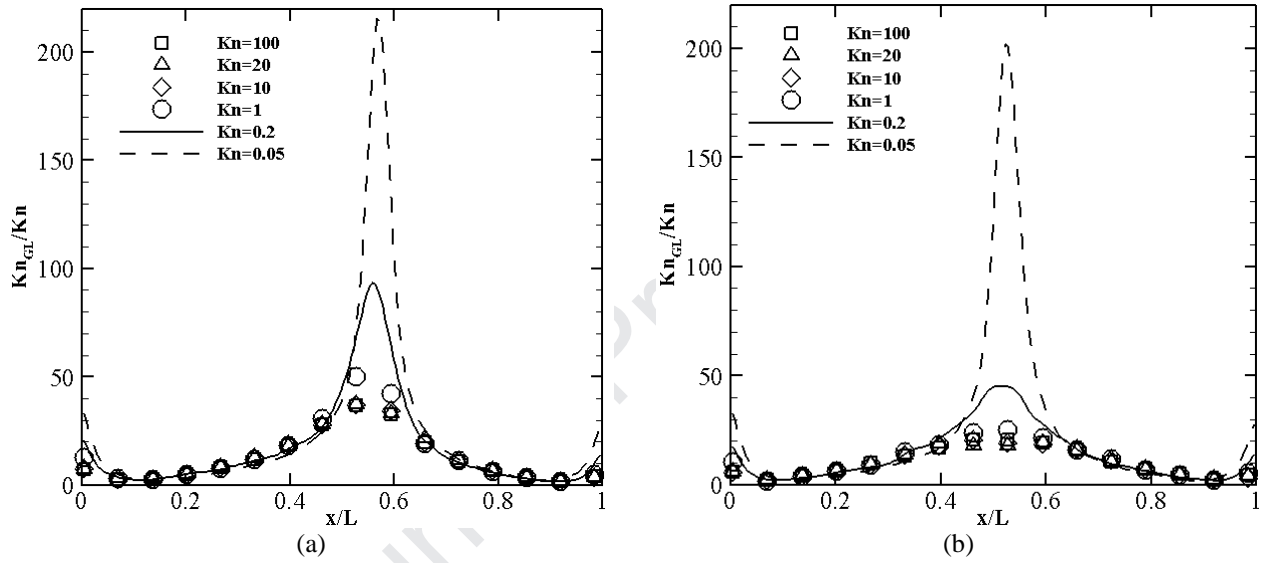


Fig. 11 $\frac{Kn_{GL}}{Kn}$ at $y=3L/4$ line for cavity flow with a) $U_w=300$ m/s b) $U_w=100$ m/s (FP prediction)

Our investigation shows the factor which influences the $\frac{Kn_{GL}}{Kn}$ is the cavity central vortex. Variation of the vortex location with the Kn is depicted in Figure 12. Viscous dissipation in the flow enlarges by increasing the Kn. In other words, the induced kinetic energy from the top lid dissipates more notably at higher Kn, which shifts the core vortex toward the downward left to the geometric center of the cavity.

Figure 12 shows that a sudden change in the location of core vortex occurs around $Kn=1$, which could be the result of Knudsen diffusion effects. In the channel flows, Knudsen diffusion phenomenon leads to a minimum mass flow rate at $Kn=1$ [34]. For $Kn>1$, rarefaction hinders

information propagation. Therefore, the variation of the core vortex becomes slower. Additionally, as the flow rarefies more, the center of the vortex moves away from the driven lid to the bottom wall [30].

Considering Figures 11 and 12, It can be known that the maximum value of $\frac{Kn_{GL}}{Kn}$ occurs around the location of the vortex center. As it is shown, it is around $x=0.55L$ for $Kn=0.05$ and by increasing Kn , it moves toward the left side, the same as vortex center.

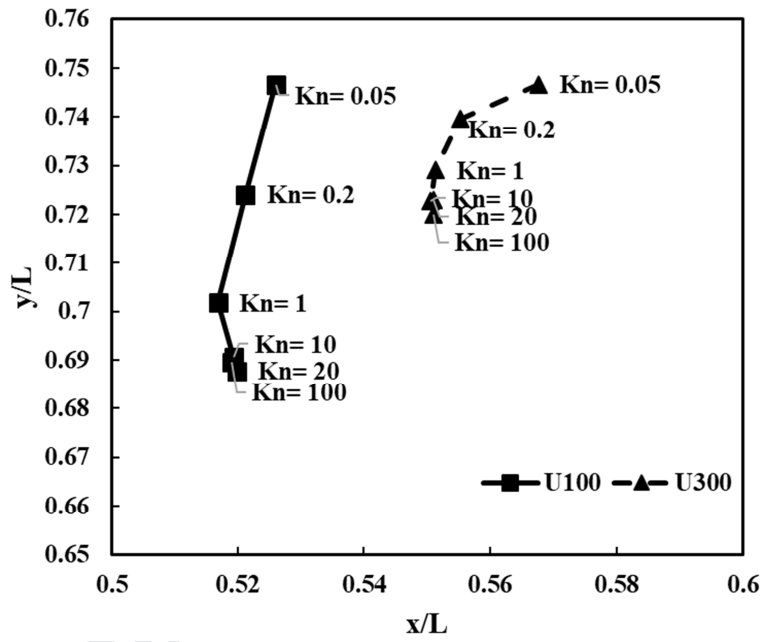


Fig. 12 Variation of the vortex location center by the Kn by FP method

The circulation of the mean velocity field, Γ is calculated as follows:

$$\Gamma = \oint V \cdot ds = \int \text{rot}_n V \cdot dA = \sum_{i,j} \left[\frac{(V_{y,i+1} - V_{y,i,j})}{\Delta x} - \frac{(V_{x,j+1} - V_{x,i,j})}{\Delta y} \right] \Delta x \Delta y \quad (36)$$

The summation is calculated over the entire domain of the cavity. Figure 13 shows the variation of flow non-dimensional circulation with the Kn in the cavity. Circulation is normalized with $\Gamma_0 = U_{wall} \times L$. It can be seen that by increasing the Kn the strength of the vortex in the cavity reduces. The reason is that there are lower collisions at high Knudsen numbers and the effects of wall velocity propagate less in the domain. Therefore, according to Figures 9 (a), (b) and 10 (a), (b), the

field velocity decreases and the gas flow becomes more uniform. Figure 13 also shows that the variation of circulation strength becomes almost constant at $Kn > 1$.

Considering Figure 11, 12 and 13, it can be deduced that vortex strength is directly related to $\frac{Kn_{GL}}{Kn}$. Increasing Kn causes weaker gas circulation and therefore $\frac{Kn_{GL}}{Kn}$ becomes smaller. As a result, $\frac{Kn_{GL}}{Kn}$ becomes more uniform and the FP solution becomes more accurate.

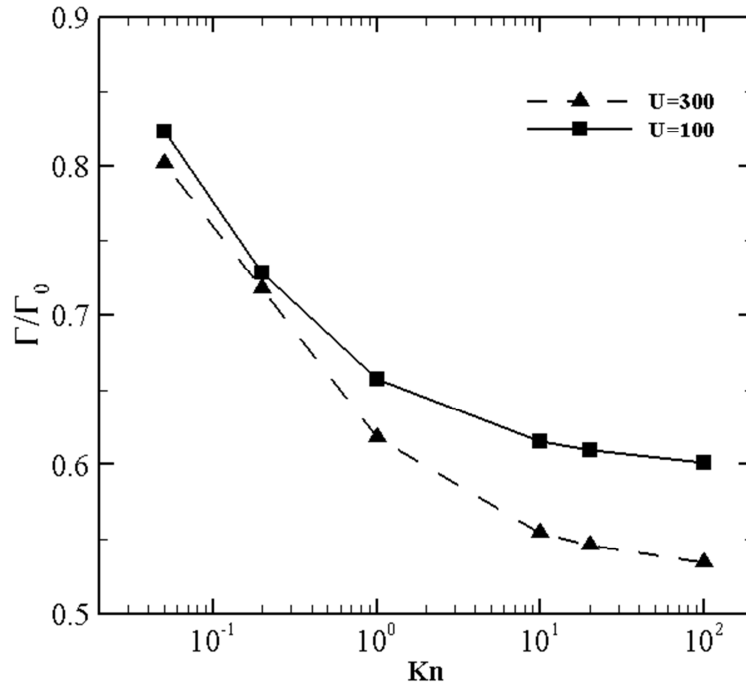


Fig. 13 Circulation of the mean velocity vector by FP method

5.3.2. Cavity cold to hot investigation

Heat transfer phenomena in the rarefied gas flow regime cannot be analyzed by continuum-based Fourier's law [37], [38]. As it is shown in Figures 14 and 15, the heat flux lines were illustrated and show cold to hot and hot to cold heat transfer predicted by the FP method.

Figure 14 shows the temperature contour with heat flux lines at different Kn for the cavity flow at $U_w=100$ m/s. The temperature is higher on the right wall due to the formation of a stagnation point on the right corner of the cavity. Additionally, by increasing Kn the particles conserve their energy obtained from lid instead of transferring it in collisions. Therefore, the temperature at the top

and right side increases by increasing Kn. The variation of temperature distribution becomes almost constant for $Kn > 1$. Evidently, by increasing Kn, the heat lines change directions from the left and bottom wall to the right side. The heat conduction equations for slightly rarefied gas are given as follows [37]:

$$q = Kn^{**} q_1 + Kn^{**2} q_2 + Kn^{**3} q_3 \quad (37)$$

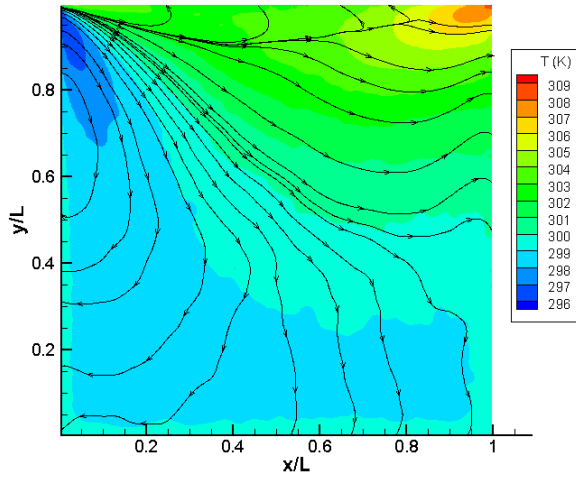
$$q_1 = 0 \quad (38)$$

$$q_2 = -\frac{5}{4} \gamma_2 \frac{\partial T^{**}}{\partial x_i} \quad (39)$$

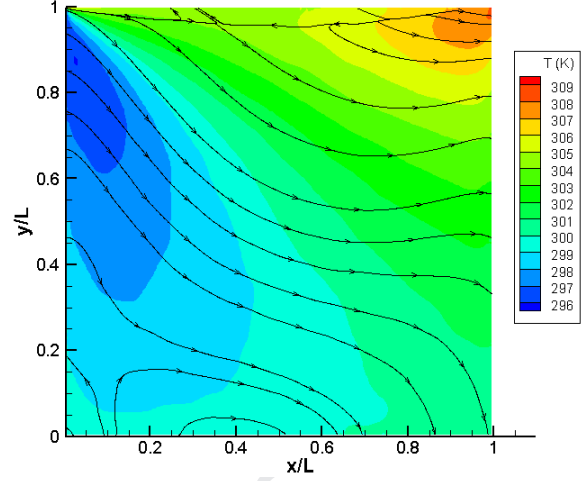
$$q_3 = -\frac{5}{4} \gamma_2 \frac{\partial T^{**}}{\partial x_i} - \frac{5}{4} \gamma_5 T^{**} \frac{\partial T^{**}}{\partial x_i} + \frac{1}{2} \gamma_3 \frac{\partial^2 u_i^{**}}{\partial x_j^2} \quad (40)$$

, where $Kn^{**} = Kn\sqrt{\pi}/2$, $T^{**} = (T - T_0)/T_0$, $u_i^{**} = u_i/\sqrt{2RT_0}$, $x_i = X_i/L$. The coefficients used in Equation (37) are set as $\gamma_2 = 1.9222$, $\gamma_3 = 1.9479$ and $\gamma_5 = 0.9611$ [37].

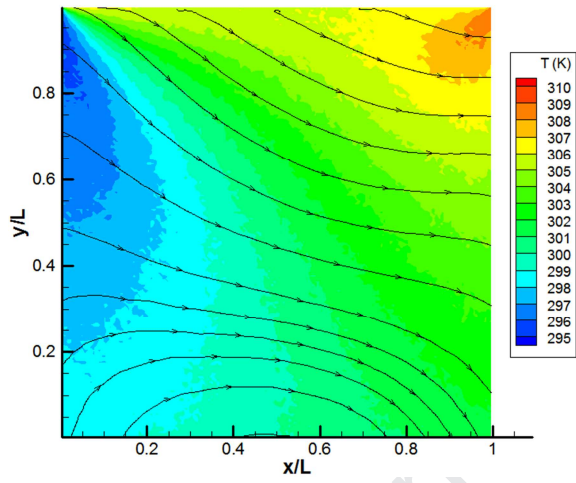
Mahdavi and Roohi [38] and Balaj et al. [39] showed that $\frac{\partial^2 u_i^{**}}{\partial x_j^2}$ is the dominant term at higher Kn regimes; while $\frac{\partial T^{**}}{\partial x_i}$ becomes more effective at lower Kn and causes hot to cold heat transfer. Therefore, as it is shown in Figure 14, by increasing Kn, the effect of the term $\frac{\partial^2 u_i^{**}}{\partial x_j^2}$ leads heat lines from left to right. On the other hand, $\frac{\partial T^{**}}{\partial x_i}$ leads the heat lines from the hot regions in the top of the cavity into the cold zones at the bottom. Therefore, the balances between these terms determine the direction of heat lines in the cavity. Similar to Ref. [40], two DSMC contours were selected to compare temperature contours with the FP solution.



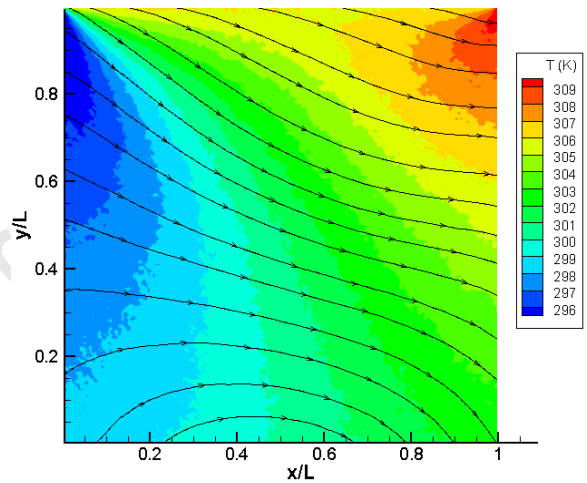
(a)



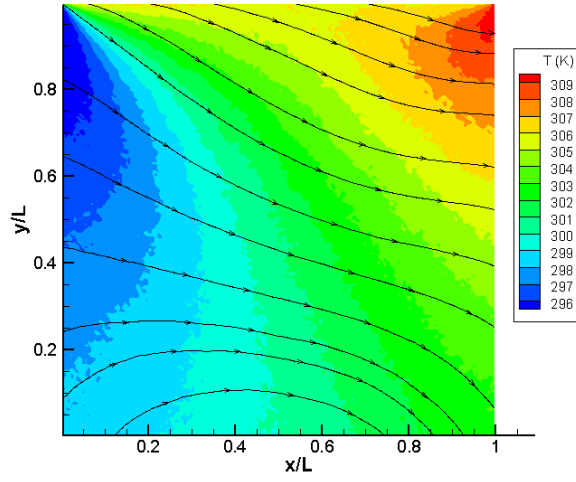
(b)



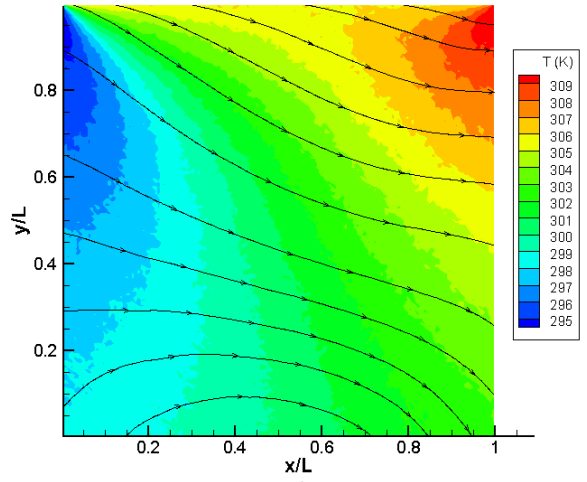
(c)



(d)



(e)



(f)

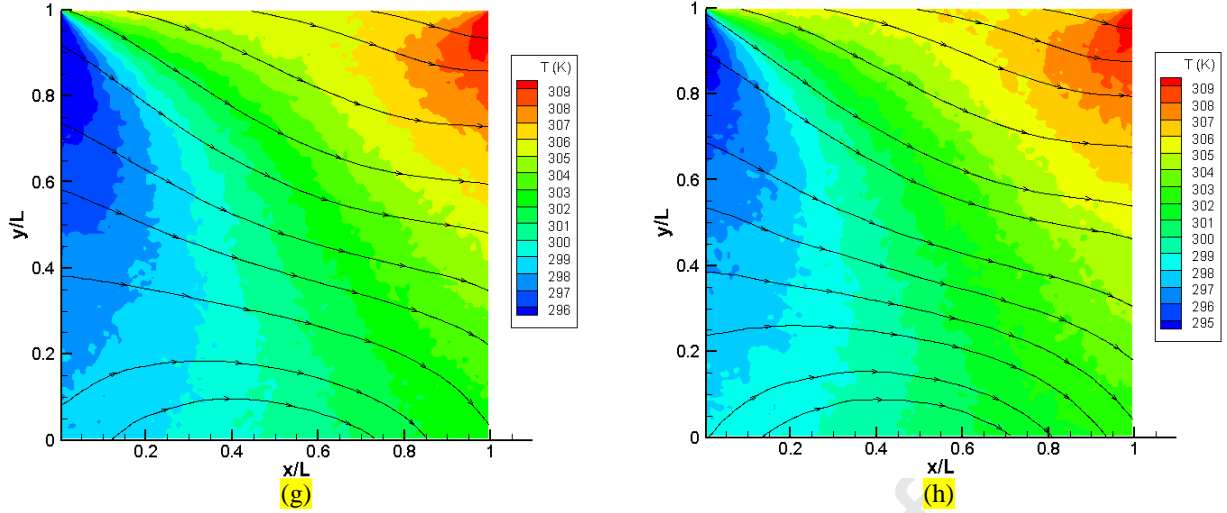
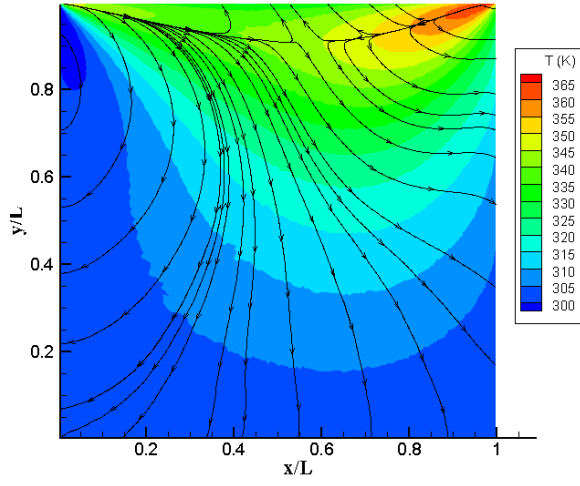
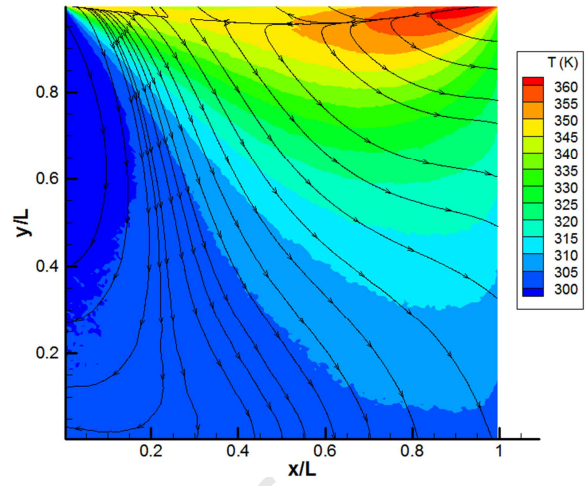


Fig. 14 Temperature contours with heat flux lines for cavity with $U_w=100$ m/s
 FP: a) $Kn=0.05$ b) $Kn=0.2$ c) $Kn=1$ d) $Kn=10$ e) $Kn=20$ f) $Kn=100$
 DSMC: g) $Kn=20$ h) $Kn=100$

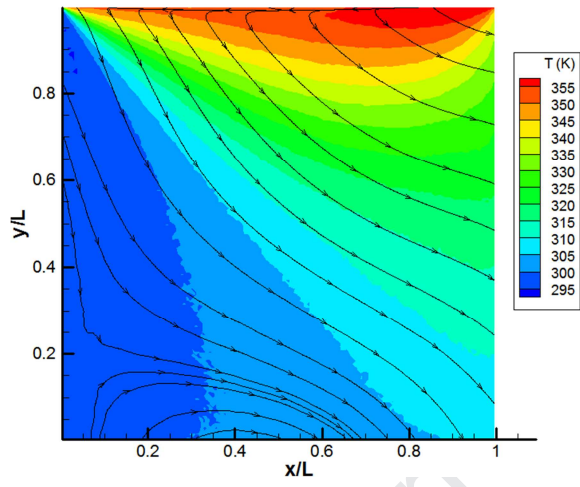
Figure 15 shows the temperature contour with heat flux line at different Kn for the cavity flow at $U_w=300$ m/s. As previously discussed, increasing Kn causes a higher temperature at the top and right wall; By comparing Figure 14 and 15, it can be concluded that at the case $U=300$ m/s the temperature near the top becomes more dominant than the right side. The reason comes back to higher kinetic energy at the cavity lid. Additionally, this kinetic energy causes a higher temperature gradient at the entire domain. Therefore, $\frac{\partial T^{**}}{\partial x_i}$ has noticeable effects on the heat lines. Thus, the heat lines tend to deviate towards the bottom. Consequently, the slope of heat lines is more on this occasion.



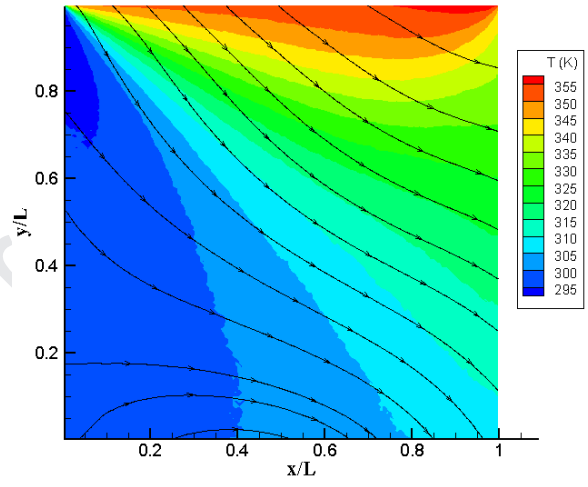
(a)



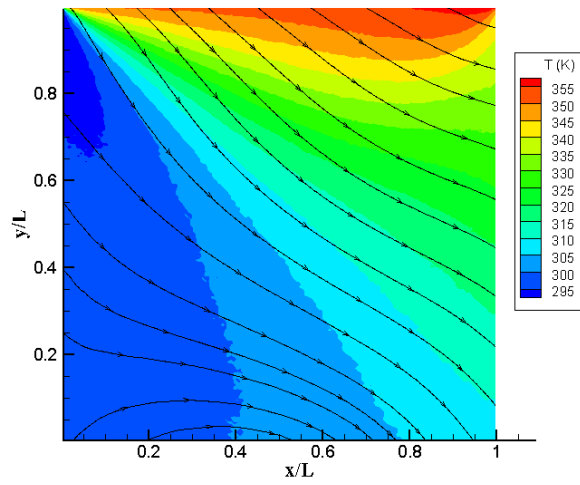
(b)



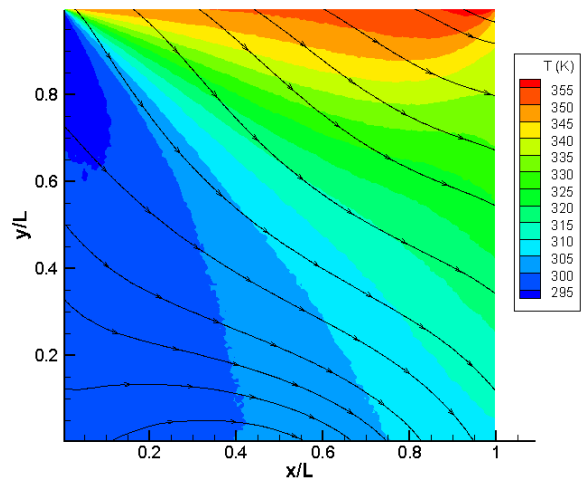
(c)



(d)



(e)



(f)

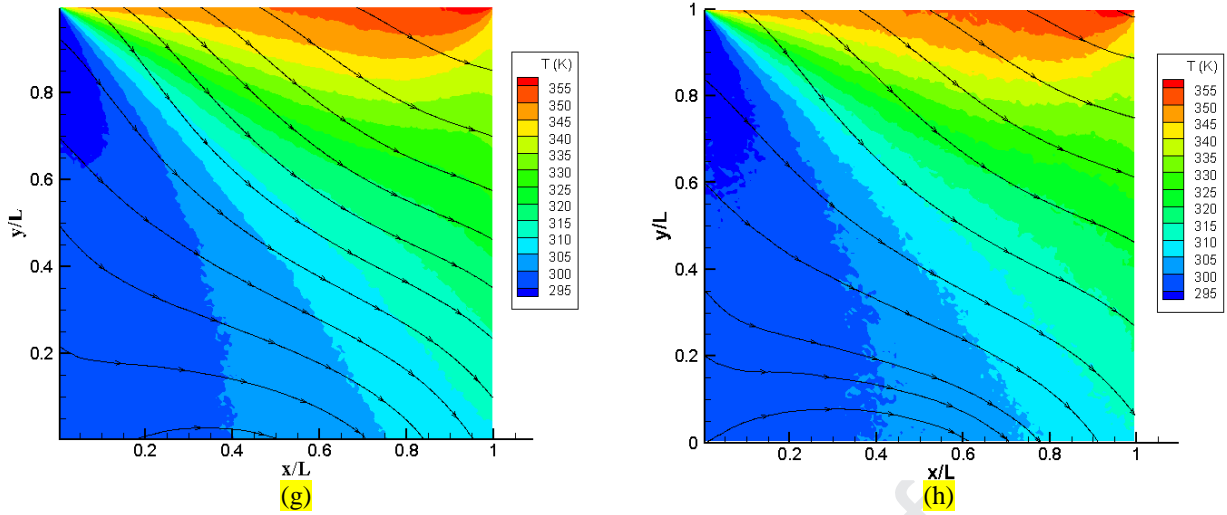


Fig. 15 Temperature contours with heat flux lines for cavity with $U_w=300$ m/s
 FP: a) $Kn=0.05$ b) $Kn=0.2$ c) $Kn=1$ d) $Kn=10$ e) $Kn=20$ f) $Kn=100$
 DSMC: g) $Kn=20$ h) $Kn=100$

Figure 16 shows various heat flux patterns, classified according to the Mach number and Kn . As can be seen, two separate regions could be classified. At lower Mach and Knudsen numbers smaller than 0.1, both cold to hot and hot to cold heat transfer are observed; this region is distinguished by black circles. Complete cold-to-hot transfer in the cavity flow occurs at low Mach and higher Knudsen numbers, distinguished by blue squares.

As it is shown in Figures 16 and 14, by increasing the Kn at low Mach, the cold to hot heat transfer increases and at high Kn , the whole cavity is covered by cold to hot heat transfer. However, at higher Mach, the entire cavity has both cold to hot and hot to cold heat transfers. The reason is that by increasing the lid velocity $\frac{\partial^2 u_i^{**}}{\partial x_j^2}$ becomes stronger; thus, kinetic energy converts to heat.

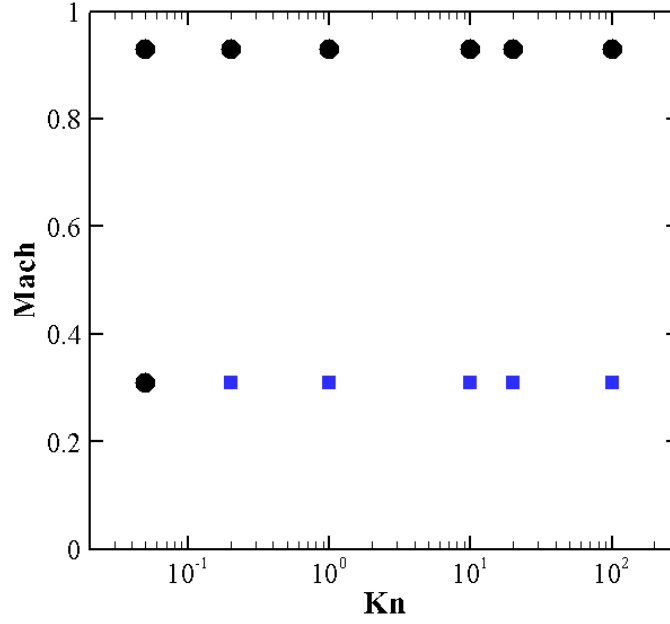


Fig. 16 Distinction of heat flux pattern in Kn-Mach plane by FP method.

5.4. Cavity Computational Cost

In DSMC, a reference time step is considered as follows [30]:

$$\Delta t_{ref} = \frac{1}{5} \frac{\lambda_{global}}{C_{mp}} \quad (41)$$

, where λ_{global} is the global mean free path and $C_{mp} = \sqrt{2kT/m}$ is the most probable speed of the gas molecules. In the DSMC method, particles are not permitted to move more than a cell length in a time step. Therefore, the minimum of transit time and the mean collision time should be selected as the appropriate time step [30].

$$\Delta t_{transit} = \frac{1}{2} \frac{L_{cell}}{C_{mp}} \quad (42)$$

$$\Delta t_{cell} = \text{Min}(\Delta t_{coll.cell}, \Delta t_{transit}) \quad (43)$$

In the FP method, the time step is calculated by Equation (44), which is a fraction of the transit time [10].

$$\Delta t_{FP} = \min\left(\frac{0.5 \times \delta x}{\sqrt{\frac{kT}{m}}}, \frac{0.5 \times \delta y}{\sqrt{\frac{kT}{m}}}\right) \quad (44)$$

Table 4 shows the time step needed for each method in the cavity flow. As it is shown, the FP works with a much larger time step, resulting in faster convergence and lower computational costs.

Table 4 Time step comparison between DSMC and FP methods in cavity flow ($U_w=300$ m/s, $Kn=1$)

Time step	Value
FP time step (s)	1.33×10^{-11}
DSMC time step (s)	1.0×10^{-12}
<i>FP Time step</i>	13.3
<i>DSMC Time step</i>	

Additionally, a comparison is made between different Knudsen numbers and wall velocities, which is reported in Table 5. As shown, the DSMC computational cost for these cases is higher than FP. As it is shown, the CPU-time ratio decreases by increasing the Kn. Also, as previously discussed, the CPU-time for each particle in FP is almost constant through all Knudsen numbers while it decreases by increasing the Kn.

Table 5 CPU-time comparison between DSMC and FP methods in Cavity flow

U_w (m/s)	Kn	$\left(\frac{\text{CPU time}}{n_p}\right)_{DSMC} (s/particle)$	$\left(\frac{\text{CPU time}}{n_p}\right)_{FP} (s/particle)$	$\frac{\text{DSMC CPU time}}{\text{FP CPU time}}$
100	10	1.05×10^{-4}	3.11×10^{-6}	3.39
	10	1.06×10^{-4}	3.63×10^{-6}	2.93
300	1	1.22×10^{-4}	3.80×10^{-6}	3.22
	0.05	1.26×10^{-4}	3.63×10^{-6}	3.47

6. Conclusion

Here, a detailed investigation of the performance and accuracy of the FP method in treating shear driven flows over a wide range of Knudsen numbers and Mach numbers is reported. According to the results obtained for the Couette flow, it is concluded that in the FP method, high-speed flows can achieve more accurate results at faster convergence. However, this method shows remarkable errors in the Knudsen layer at low-speed flows with high Knudsen numbers. Maximum error occurs

in heat flux and it is around 9% of q_0 . It is understood that in the FP method, the computational cost is independent of the Knudsen number. While in the DSMC approach, the CPU-time depends directly on the number of intermolecular collisions. By decreasing the Knudsen number, the number of collisions decreases. Therefore, it causes a slower convergence and more computational cost.

Different limits of the Knudsen number in the continuum, transition, and free molecular flow in the subsonic and supersonic regimes was investigated. In the cavity flow, our results indicate that the Fokker Planck method predicts with errors at lower Knudsen numbers. The reason is stronger circulating flows at lower Kn regimes, which cause more non-equilibrium effects in the geometry. By increasing Kn, the vortex becomes weaker and therefore, there is more consistency between the DSMC and FP solutions. Thermal behavior was also studied in this paper. It was shown that by increasing the Kn, the heat lines are directed to the bottom of the cavity due to increasing non-equilibrium effects. Additionally, computational cost was reported in this paper. The change in Kn has not any considerable effect on the FP cost; while it is a crucial factor in the DSMC. It is shown that the accuracy of the FP and CPU-time improves by increasing the lid velocity.

Nomenclature

A	Drift coefficient
D	Diffusion coefficient
e	Internal energy (kJkg^{-1})
E	Relative error
F	Mass distribution function
G	External force
k	Boltzmann constant (K^{-1})
Kn	Knudsen number
L	Flow characteristic length (m)
m	Particle molecular mass (kg)
M	Particle velocity (ms^{-1})
Ma	Mach number
N	Number of molecules
P	Pressure ($\text{kgm}^{-1}\text{s}^{-2}$)

PPC	Particle per cell
Pr	Prandtl number
q	Thermal flux (Wm^{-2})
Re	Reynolds number
t	Time (s)
T	Temperature (K)
u_j	Velocity in x direction (ms^{-1})
U	Cell velocity (ms^{-1})
v_j	Velocity in y direction (ms^{-1})
x(t)	Particle position (m)

Greek

δ	Mean molecular distance (m)
Δt	Time step (s)
Δx	Grid size (m)
λ	Mean molecular free path (m)
Λ	Stability factor
μ	Dynamic viscosity ($\text{kgm}^{-1}\text{s}^{-1}$)
ξ	Non-dimensional independent variables
π	Stress tensor
ρ	Density (kgm^{-3})
τ	Time constant

Superscript

Boltz	Boltzmann
FP	Fokker Planck

Subscript

coll	Collision
initial	Initial
ref	Reference
w	wall

References

- [1] H.-S. Tsien, "Superaerodynamics, mechanics of rarefied gases," *J. Aeronaut. Sci.*, vol. 13, no. 12, pp. 653–664, 1946.
- [2] P. A. Chambre and S. A. Schaaf, *Flow of rarefied gases*, vol. 4971. Princeton University Press, 2017.

- [3] G. Karniadakis, A. Beskok, and N. Aluru, *Microflows and nanoflows: fundamentals and simulation*, vol. 29. Springer Science & Business Media, 2006.
- [4] E. Y. Moghadam, E. Roohi, and J. A. Esfahani, “Heat transfer and fluid characteristics of rarefied flow in thermal cavities,” *Vacuum*, vol. 109, pp. 333–340, 2014.
- [5] G. A. Bird, “Approach to translational equilibrium in a rigid sphere gas,” *Phys. fluids*, vol. 6, pp. 1518–1519, 1963.
- [6] J. G. Kirkwood, “The statistical mechanical theory of transport processes I. General theory,” *J. Chem. Phys.*, vol. 14, no. 3, pp. 180–201, 1946.
- [7] C. Cercignani, “The boltzmann equation,” in *The Boltzmann equation and its applications*, Springer, 1988, pp. 40–103.
- [8] P. Jenny, M. Torrilhon, and S. Heinz, “A solution algorithm for the fluid dynamic equations based on a stochastic model for molecular motion,” *J. Comput. Phys.*, vol. 229, no. 4, pp. 1077–1098, 2010.
- [9] M. H. Gorji, M. Torrilhon, and P. Jenny, “Fokker–Planck model for computational studies of monatomic rarefied gas flows,” *J. Fluid Mech.*, vol. 680, pp. 574–601, 2011.
- [10] M. H. Gorji and P. Jenny, “An efficient particle Fokker–Planck algorithm for rarefied gas flows,” *J. Comput. Phys.*, vol. 262, pp. 325–343, 2014.
- [11] S. K. Singh, C. Thantapally, and S. Ansumali, “Gaseous microflow modeling using the Fokker-Planck equation,” *Phys. Rev. E*, vol. 94, no. 6, p. 63307, 2016.
- [12] M. H. Gorji and P. Jenny, “A device concept for demixing of gas species based on excitation of internal energy modes,” in *ASME 2013 11th International Conference on Nanochannels, Microchannels, and Minichannels*, 2013, p. V001T12A011-V001T12A011.
- [13] H. Gorji and P. Jenny, “Continuous stochastic equations for diatomic rarefied gas flows,” in *APS Meeting Abstracts*, 2011.
- [14] M. H. Gorji and P. Jenny, “A Fokker–Planck based kinetic model for diatomic rarefied gas

- flows,” *Phys. fluids*, vol. 25, no. 6, p. 62002, 2013.
- [15] H. Gorji and P. Jenny, “A kinetic model for gas mixtures based on a Fokker-Planck equation,” in *Journal of Physics: Conference Series*, 2012, vol. 362, no. 1, p. 12042.
- [16] H. Gorji and P. Jenny, “A generalized stochastic solution algorithm for simulations of rarefied gas flows,” in *2nd European Conference on Microfluidics (μFlu’10)*, 2010.
- [17] S. V. Bogomolov, “On Fokker-Planck model for the Boltzmann collision integral at the moderate Knudsen numbers,” *Math. Model. Comput. Simulations*, vol. 1, no. 6, p. 739, 2009.
- [18] F. Fei and J. Fan, “A diffusive information preservation method for small Knudsen number flows,” *J. Comput. Phys.*, vol. 243, pp. 179–193, 2013.
- [19] S. K. Singh and S. Ansumali, “Fokker-Planck model of hydrodynamics,” *Phys. Rev. E*, vol. 91, no. 3, p. 33303, 2015.
- [20] J. Mathiaud and L. Mieussens, “A Fokker-Planck model of the Boltzmann equation with correct Prandtl number,” *J. Stat. Phys.*, vol. 162, no. 2, pp. 397–414, 2016.
- [21] E. Jun, M. Pfeiffer, L. Mieussens, and M. H. Gorji, “Comparative study between cubic and ellipsoidal Fokker-Planck kinetic models,” *AIAA J.*, vol. 57, no. 6, pp. 2524–2533, 2019.
- [22] T. Jiang, C. Xia, and W. Chen, “An improved hybrid particle scheme for hypersonic rarefied-continuum flow,” *Vacuum*, vol. 124, pp. 76–84, 2016.
- [23] E. Jun, “Cubic Fokker-Planck-DSMC hybrid method for diatomic rarefied gas flow through a slit and an orifice,” *Vacuum*, vol. 159, pp. 125–133, 2019.
- [24] P. Jenny, S. Küchlin, and H. Gorji, “Controlling the bias error of Fokker-Planck methods for rarefied gas dynamics simulations,” *Phys. Fluids*, vol. 31, no. 6, p. 62005, 2019.
- [25] R. F. Pawula, “Approximation of the linear Boltzmann equation by the Fokker-Planck equation,” *Phys. Rev.*, vol. 162, no. 1, p. 186, 1967.
- [26] H. Risken, “The Fokker-Planck equation, volume 18 of,” *Springer Ser. Synerg.*, 1989.
- [27] C. Truesdell and R. G. Muncaster, *Fundamentals of Maxwell’s Kinetic Theory of a Simple*

Monatomic Gas: Treated as a Branch of Rational Mechanics, vol. 83. Academic Press, 1980.

- [28] A. Mohammadzadeh, E. Roohi, H. Niazmand, S. Stefanov, and R. S. Myong, “Thermal and second-law analysis of a micro-or nanocavity using direct-simulation Monte Carlo,” *Phys. Rev. E*, vol. 85, no. 5, p. 56310, 2012.
- [29] E. Taheri, E. Roohi, and S. Stefanov, “On the convergence of the simplified Bernoulli trial collision scheme in rarefied Fourier flow,” *Phys. Fluids*, vol. 29, no. 6, p. 62003, 2017.
- [30] A. Mohammadzadeh, E. Roohi, and H. Niazmand, “A parallel DSMC investigation of monatomic/diatomic gas flows in a micro/nano cavity,” *Numer. Heat Transf. Part A Appl.*, vol. 63, no. 4, pp. 305–325, 2013.
- [31] E. Roohi, V. Shahabi, and A. Bagherzadeh, “On the vortical characteristics and cold-to-hot transfer of rarefied gas flow in a lid driven isosceles orthogonal triangular cavity with isothermal walls,” *Int. J. Therm. Sci.*, vol. 125, pp. 381–394, 2018.
- [32] H. Akhlaghi, E. Roohi, and S. Stefanov, “Ballistic and Collisional Flow Contributions to Anti-Fourier Heat Transfer in Rarefied Cavity Flow,” *Sci. Rep.*, vol. 8, no. 1, p. 13533, 2018.
- [33] J. A. Esfahani, O. Ejtehad, and E. Roohi, “Second law analysis of micro/nano Couette flow using direct simulation Monte Carlo method,” *Int. J. Exergy*, vol. 13, no. 3, pp. 320–342, 2013.
- [34] E. Roohi and S. Stefanov, “Collision partner selection schemes in DSMC: From micro/nano flows to hypersonic flows,” *Phys. Rep.*, vol. 656, pp. 1–38, 2016.
- [35] T. M. M. Homolle and N. G. Hadjiconstantinou, “A low-variance deviational simulation Monte Carlo for the Boltzmann equation,” *J. Comput. Phys.*, vol. 226, no. 2, pp. 2341–2358, 2007.
- [36] E. Roohi and M. Darbandi, “Hybrid dsmc/Navier-Stokes solution of rarefied micro-nano flows,” in *Proceedings of the 2nd GASMEMS Workshop-Les Embiez*, 2010.
- [37] Y. Sone, *Molecular gas dynamics: theory, techniques, and applications*. Springer Science &

Business Media, 2007.

- [38] A.-M. Mahdavi and E. Roohi, "Investigation of cold-to-hot transfer and thermal separation zone through nano step geometries," *Phys. Fluids*, vol. 27, no. 7, p. 72002, 2015.
- [39] M. Balaj, E. Roohi, and A. Mohammadzadeh, "Regulation of anti-Fourier heat transfer for non-equilibrium gas flows through micro/nanochannels," *Int. J. Therm. Sci.*, vol. 118, pp. 24–39, 2017.
- [40] C. Christou and S. K. Dadzie, "An investigation of heat transfer in a cavity flow in the noncontinuum regime," *J. Heat Transfer*, vol. 139, no. 9, p. 92002, 2017.

- First report on the evaluation of the Fokker-Plank scheme at high Knudsen shear-driven flows
- A thorough study of the numerical efficiency of the FP scheme at various Kn and Mach numbers
- Presenting a novel parameter in detecting the border of the accuracy of the FP scheme

Competing interest: The authors declare no competing interests, either financially or in other forms.

Journal Pre-proof